BLTP3A is associated with membranes of the late endocytic pathway and is an effector of CASM

Short title: BLTP3A: a late endocytic factor and CASM effector

Michael G. Hanna[1-5], Hely O. Rodriguez Cruz[1-5], Kenshiro Fujise[1-5], Yumei Wu[1-5], C. Shan Xu[6], Song Pang[7], Zhuonging Li[8], Mara Monetti[8], Pietro De Camilli*[1-5]

[1]Department of Neuroscience, Yale University School of Medicine, New Haven, CT;

[2]Department of Cell Biology, Yale University School of Medicine, New Haven, CT;

[3]Howard Hughes Medical Institute, Yale University School of Medicine, New Haven, CT;

[4]Program in Cellular Neuroscience, Neurodegeneration and Repair, Yale University School of Medicine, New Haven, CT;

[5]Aligning Science Across Parkinson's (ASAP) Collaborative Research Network, Chevy Chase, MD;

[6]Department of Cellular and Molecular Physiology, Yale University School of Medicine, New Haven, CT;

[7]Yale University School of Medicine, New Haven, CT;

[8]Proteomics Core Facility, Sloan Kettering Institute, Memorial Sloan Kettering Cancer Center, New York, NY.

*Correspondence to Pietro De Camilli: pietro.decamilli@yale.edu

Keywords

Bridge-like lipid transfer protein, BLTP, BLTP3A, BLTP3B, Rab7, lysosome, lysosomal membrane damage, CASM, mATG8, LLOMe, LRRK1, LRRK2, Rab45

Teaser

BLTP3A is localized on membranes of the late endocytic system and is CASM effector, pointing to a role of this proteins in the response to lysosome damage

ABSTRACT

Recent studies have identified a family of rod-shaped proteins thought to mediate lipid transfer at intracellular membrane contacts by a bridge-like mechanism. We show one such protein, BLTP3A/UHRF1BP1 binds VAMP7 vesicles via its C-terminal region and anchors them to lysosomes via the binding of its chorein domain containing N-terminal region to Rab7. Upon lysosome damage and resulting mATG8 recruitment to their surface by CASM, BLTP3A first dissociates from lysosomes but then reassociates with them via an interaction of its LIR motif with mATG8. Such interaction is mutually exclusive to the binding of BLTP3A to vesicles and leaves its N-terminal chorein domain, i.e. the proposed entry site of lipids into this family of proteins, available for binding to another membrane, possibly the ER. Loss of BLTP3A increases the lysis of lysosomes in response to damage. Our findings reveal that BLTP3A is an effector of CASM, potentially as part of a mechanism to help repair or minimize lysosome damage by delivering lipids.

INTRODUCTION

Eukaryotic cells are populated by anatomically discontinuous lipid-based intracellular membranes and thus require mechanisms to transfer lipids between them. This is achieved both by membrane traffic (Palade, 1975) and by lipid transfer proteins (LTPs) (DeGrella and Simoni, 1982; Wirtz, 1991; Reinisch et al., 2024) or protein complexes that have the property to extract lipid from membranes, shield them in hydrophobic cavities and insert them into acceptor membranes. Typically, LTPs function at sites where two membranes are closely apposed, i.e. where transfer may occur with greater speed and specificity (Saheki and Camilli, 2017; Wong et al., 2019; Prinz et al., 2020; Voeltz et al., 2024). Moreover, in most cases studied so far transfer occurs via a shuttle mechanism in which a lipid harboring module that contains one or few lipids, is connected via flexible linkers to protein domains that tether the two membranes together (Prinz et al., 2020; Reinisch et al., 2024). In recent years, however, the occurrence of an additional mode of lipid transfer, mediated by rod-like proteins that harbor a hydrophobic groove or tunnel along which lipids can slide and which directly bridge two membranes has been described (Kumar et al., 2018; Osawa et al., 2019; Maeda et al., 2019; Valverde et al., 2019; Wong et al., 2019; Li et al., 2020; Leonzino et al., 2021; Dziurdzik and Conibear, 2021; Cai et al., 2022a; Hanna et al., 2022; Adlakha et al., 2022; Kang et al., 2024; Banerjee et al., 2024). These proteins, collectively referred to as bridge-like lipid transfer proteins (BLTPs), are evolutionary related and have a similar basic molecular architecture (Leonzino et al., 2021; Neuman et al., 2022; Levine, 2022; Hanna et al., 2023). Their core is represented by concatemers of small beta-sheets with a taco-like fold, referred to as repeating beta-groove (RBG) modules (Levine, 2022; Hanna et al., 2023), which are lined by hydrophobic amino acids (a.a.) at their inner surface, thus generating a continuous hydrophobic surface (Kumar et al., 2018; Li et al., 2020; Levine, 2022; Neuman et al., 2022; Hanna et al., 2023; Kang et al., 2024; Wang et al., 2024b). Moreover, they comprise motifs or domains that allow them to tether two different membranes and a variety of loops or outpocketings of variable length which may have regulatory or protein-protein interaction functions (Kumar et al., 2018; Dziurdzik and Conibear, 2021; Guillén-Samander et al., 2021; Neuman et al., 2022; Adlakha et al., 2022; Guillén-Samander et al., 2022; Hanna et al., 2023; Kang et al., 2024; Wang et al., 2024a; b). They are thought to mediate bulk lipid (generally phospholipid) transfer between membranes. As the groove at its narrowest point can only accommodate one phospholipid, such transport is thought to be unidirectional (Li et al., 2020; Kang et al., 2024; Wang et al., 2024b). BLTPs comprise VPS13, the founding member of the family, as well as the autophagy factor ATG2, and other proteins originally referred to by multiple different names in different organisms and are now renamed BLTP1, BLTP2 and BLTP3 (Neuman et al., 2022; Hanna et al., 2023). These proteins differ in the number of RBG modules and thus in length: 17 in BLTP1, the longer member of the family and six in BLTP3, the shorter family member (Levine, 2022).

The putative role of BLTPs in bulk lipid transfer is ideally suited for membrane bilayer expansion or repair via the delivery of newly synthesized lipids from the ER, a possibility strongly supported by the well-established roles of yeast VPS13 in the growth of the sporulation membrane (Park and Neiman, 2012) and of ATG2 in the expansion of the isolation membrane (Wang et al., 2001; Velikkakath et al., 2012; Gómez-Sánchez et al., 2018; Osawa et al., 2019; Valverde et al., 2019). Other processes in which BLTPs anchored to the ER have been implicated also involve

membrane expansion, such as biogenesis of mitochondria and of peroxisomes (Park et al., 2016; John Peter et al., 2017; Anding et al., 2018; Baldwin et al., 2021; Guillén-Samander et al., 2021), organelles not connected to the ER by membrane traffic. In other cases, the relation of the putative bulk lipid transfer function of BLTPs to bilayer expansion is less clear, and BLTPs seem to be primarily important to control the composition of the receiving bilayer (Tokai et al., 2000; John Peter et al., 2022; Wang et al., 2022; Hanna et al., 2022; Banerjee et al., 2024). In this case delivery of new lipids to a membrane may be removed by a compensatory mechanism, for example by membrane traffic, thereby limiting expansion overall. As BLTPs have been identified only recently, much remains to be discovered about their function.

Two very similar BLTPs of which little is known are BLTP3A (also called UHRF1BP1) and BLTP3B (also called SHIP164 or UHRF1BP1L for UHRF1BP1-Like) (Hanna et al., 2022; Neuman et al., 2022). BLTP3A was originally identified as a Binding Protein (BP) of the epigenetic regulator UHRF1 (Unoki et al., 2004) while its paralogue BLTP3B was independently identified as an interactor of syntaxin 6 (Syntaxin 6 Habc-interacting protein of 164 kDa, hence its alias SHIP164) and found to localize on membrane of the endocytic pathway harboring this SNARE protein (Otto et al., 2010). BLTP3A and BLTP3B were also top hits in a screen for effectors of Rab7 and Rab5, respectively (Gillingham et al., 2019).

Following up on these earlier studies we have recently reported a systematic characterization of the properties of BLTP3B (Hanna et al., 2022). We showed that endogenous BLTP3B is localized on clusters of endocytic vesicles that interact with components of the retrograde microtubule-based transport system [dynein light chain (DYNLL1/2) (Carter et al., 2016) and Rab45 (CRACR2a) (Wang et al., 2019)] and that loss of BLTP3B results in a perturbation of the retrograde traffic to the Golgi area of the cation independent mannose-6-phosphate receptor (MPR) (Lin et al., 2003). Exogenous expression of BLTP3B, leading to its overexpression, resulted in a striking accumulation of these vesicles that formed tightly packed clusters anchored to Rab5-positive early endosomes (Hanna et al., 2022). How the putative lipid transfer function of BLTP3B relate to this localization and phenotypes remains an open question.

The goal of the present study was to acquire new information about BLTP3A, a risk gene for lupus erythematosus (Gateva et al., 2009; Zhang et al., 2011; Wen et al., 2020). We report here that BLTP3A, like BLTP3B, is localized on clusters of small vesicles and that its overexpression induces a massive expansion of such clusters. However, while clusters of BLTP3B-positive vesicles are anchored to Rab5-positive organelles, clusters of BLTP3A-positive vesicles are anchored to LAMP1-positive organelles via Rab7. We further show that lysosome damage triggers the rapid loss of the Rab7-dependent association of BLTP3A with LAMP1-positive organelles, followed by its CASM (Durgan and Florey, 2022)-dependent reassociation with them in an mATG8 and LIR motif-dependent way. These findings have implications for lysosome health, as perturbation of their membranes reveals a faster lysis in BLTP3A KO cells than in control cells. Collectively, these findings point to a role of this protein at the interface between late endocytic traffic and lysosomes and also raise the possibility that BLTP3A, via its lipid transport functions, may play a role in the response to lysosome damage.

148 **RESULTS**
149
150 **Close structural similarity, but different interactions, of BLTP3A relative to BLTP3B**
151
152 BLTP3A is very similar to BLTP3B (41% identity and 58% positives in primary sequence).
153 Moreover, fold-prediction algorithms (Jumper et al., 2021; Yang et al., 2020) show that BLTP3A
154 shares all the key structural features of BLTP3B: a rod-like core composed by six RBG motifs
155 (Levine, 2022), a hydrophobic groove that runs along its entire length, a large disordered
156 outpocketing of the rod-like core (a.a. 885-1188) and a C-terminal helix (a.a. 1394-1440) (**Figure**
157 **1A**). Both BLTP3A and BLTP3B are reported in Biogrid (https://thebiogrid.org) to be interactors
158 of Rab45 (CRACR2a), an adaptor for dynein and retrograde microtubule traffic (Wang et al., 2019)
159 and, accordingly, over-expression of GFP-Rab45 in RPE1 cells (?) concentrated BLTP3A-mRFP
160 to perinuclear spots (the centrosomal area) similar to our previous findings of BLTP3B
161 (**Supplemental Figure 1A**) (Hanna et al., 2022). Despite these similarities, BLTP3A lacks the
162 motifs responsible for binding to syntaxin-6 (Stx6) and the dynein light chain (DYNLL1/2) (**Figure**
163 **1B**), which we had identified in BLTP3B (Hanna et al., 2022). Moreover, BLTP3A was shown to
164 be an effector of Rab7, instead of Rab5 (Gillingham et al., 2019). A per-residue evolutionary
165 conservation analysis of BLTP3A carried out using the ConSurf server (Armon et al., 2001; Yariv
166 et al., 2023) revealed that most conserved residues belong to the RBG motif core, particularly its
167 N-terminal portion (**Figure 1A**). Short stretches of conserved residues, however, are also present
168 in predicted unfolded loops emerging from this core, including the large outpocketing. As revealed
169 by western blotting, BLTP3A, like BLTP3B, has broad expression in different mouse tissues
170 (**Figure 1C**), with higher levels occurring in brain and lung.
171
172 **BLTP3A localizes to foci concentrated near lysosomes**
173
174 In a previous preliminary analysis of BLTP3A localization (Hanna et al., 2022) we had shown that
175 exogenously expressed fluorescently tagged BLTP3A appears as fluorescent foci localized in
176 proximity of organelles positive for the lysosome marker LAMP1 and of Rab7, a Rab associated
177 with late endosome and lysosomes (these organelles will be referred to henceforth collectively as
178 "lysosomes"). As our study of BLTP3B had shown that its exogenous expression resulted in an
179 enlargement of the BLTP3B positive compartment (vesicle clusters), we wished to confirm that
180 even endogenous BLTP3A was localized in proximity of lysosomes. Available antibodies directed
181 against BLTP3A did not detect a clear specific signal by immunocytochemistry. Thus, we turned
182 to a knock-in strategy to epitope tag the endogenous protein. Since preliminary experiments
183 revealed heterogeneity in the expression levels of BLTP3A in frequently used cell lines, we chose
184 A549 cells (lung adenocarcinoma epithelial cells) for these experiments where we detected robust
185 expression of BLTP3A, consistent with high expression of BLTP3A in the lung (**Figure 1C**).
186
187 The BLTP3A locus in A549 cells was edited by inserting after residue V904 a nucleotide sequence
188 encoding a single V5 epitope flanked on either side with short GSGSG linkers (**Supplemental**
189 **Figure 1B**). This site is within a predicted disordered region and is not expected to change the
190 lipid channel core of BLTP3A **(Supplemental Figure 1C).** Edited BLTP3A was validated by

Western blotting of homogenates of edited cells revealing a V5-positive band (endogenous BLTP3A^V5) with the same motility as BLTP3A (**Figure 1D**).

Anti-V5 immunofluorescence of edited cells showed small weakly fluorescence puncta throughout the cytoplasm, which were enriched in central regions of cells (**Figure 1E**) and were not observed in WT cells immunostained under the same conditions (**Figure 1E**). Importantly, many V5-positive puncta were adjacent to, or partially overlapping with, the fluorescence produced by antibodies against LAMP1 (**Figure 1E**), consistent with BLTP3A being a Rab7 effector. The fluorescence of exogenously expressed tagged BLTP3A-GFP overlapped with anti-V5 immunofluorescence of edited cells, in agreement with our previous preliminary findings (Hanna et al., 2022), although accumulations of BLTP3A-GFP fluorescence were much larger (**Figure 1E**).

Large BLTP3A foci produced by BLTP3A overexpression represent clusters of vesicles anchored to lysosomes

Given the similar localization of endogenous and exogenous BLTP3A next to lysosomes, we capitalized on exogenous BLTP3A tagged with various fluorescently tagged proteins, i.e. constructs which could be analyzed by Correlative Light-Electron Microscopy (CLEM) (immunofluorescence of the V5 epitope requires fixation and permeabilization, i.e. a treatment that perturbs cell ultrastructure). We primarily used RPE-1 cells for these studies, as LAMP1-positive organelles in these cells are very large, abundant, clustered around the Golgi complex and nucleus (**Figure 1F**), and thus easy to identify by microscopy even without specific markers. Upon co-expression of LAMP1-GFP and BLTP3A-mRFP (**Figure 1G**), two sets of BLTP3A-mRFP-positive structures were observed by fluorescence microscopy: i) BLTP3A-mRFP accumulations directly adjacent to lysosomes, often bridging two closely apposed LAMP1-GFP-vacuoles and ii) larger (often very large) BLTP3A-mRFP accumulations not obviously connected to the large LAMP1-GFP-vacuoles. Analysis of these structures by CLEM in RPE-1 cells also expressing mito-BFP (to help fluorescence - EM alignment) showed that BLTP3A-mRFP foci represented tightly packed clusters of approximately 50-70 nm vesicles (**Figure 1H**). Importantly, the vesicles of such clusters directly adjacent to LAMP1-GFP vacuoles appeared to be tethered to lysosomal membranes, with an average distance of ~10-11 nm (**Figure 1I**).

This exaggerated accumulation of large clusters of small vesicles mirrors what we had observed upon overexpression of BLTP3B, indicating that a shared property of BLTP3A and BLTP3B is to bind small vesicles, induce their accumulation, cluster them, and anchor such clusters to other organelles although clusters of BLTP3B vesicles are anchored to early endosomes (consistent with BLTP3B being an effector of Rab5), while clusters of BLTP3A are anchored to late endosomes/lysosomes (consistent with BLTP3A being an effector of Rab7). As our study of BLTP3B had shown that even BLTP3B expressed at an endogenous level is localized to vesicle clusters which are much smaller than clusters observed upon BLTP3B overexpression (Hanna et al., 2022), we hypothesized that the massive accumulation of vesicles observed upon overexpression of BLTP3 isoforms reflect a property of these proteins to nucleate biomolecular condensates. Accordingly, live imaging revealed that both clusters of BLTP3A and of BLTP3B

(see Video 1 and Figure 8E from Hanna et al., 2022) are highly dynamic. For example, they can undergo fission into smaller clusters, as expected for a compartment with liquid-like properties.

BLTP3A positive vesicles contain VAMP7, a SNARE implicated in traffic to lysosomes

The clustering of BLTP3A-positive vesicles next to lysosomes suggested that they may represent organelles destined to fuse with them, perhaps arrested at a docking stage due to a dominant negative effect of BLTP3A overexpression. As at least some of the vesicles that fuse with late endosomes and lysosomes harbor VAMP7 in their membrane (Advani et al., 1999; Pols et al., 2013), we explored the potential presence of this SNARE in BLTP3A-positive vesicles (**Figure 1J**). Supporting this hypothesis, anti-VAMP7 immunofluorescence revealed a striking overlap with the fluorescence of BLTP3A-mRFP both on the isolated BLTP3A clusters and on those anchored to lysosomes (**Figure 1J**). A similar overlap was observed between the BLTP3A signal and immunofluorescence for VAMP4 (**Figure 1J**), another SNARE protein implicated in endosomal traffic (Martinez-Arca et al., 2001; Mallard et al., 2002; Tran et al., 2007). In spite of the many similarities between BLTP3A and BLTP3B, no fluorescence overlap was observed between BLTP3B-mRFP fluorescence and endogenous VAMP7 or VAMP4 immunoreactivity (**Supplemental Figure 1D**), revealing major differences in the cargo of BLTP3A and BLTP3B vesicles. However, BLTP3A-mRFP accumulations also overlapped with the immunofluorescence of endogenous ATG9A, a component of autophagosome precursor vesicles, (**Figure 1J**), as previously observed for BLTP3B-mRFP (Hanna et al., 2022) (**Supplemental Figure 1D**). As both VAMP4 and VAMP7 were reported to interact with LRRK1 and LRRK2 (Wang et al., 2018; Filippini et al., 2023), we also examined whether GFP-LRRK1 or GFP-LRRK2 can colocalize with these vesicles. While GFP-LRRK1 and GFP-LRRK2 had primarily a diffuse cytosolic localization in control cells, in a fraction of BLTP3A-mRFP expressing cells they strikingly colocalized with BLTP3A-positive accumulations (**Supplemental Figure 1E-G, Supplemental Figure 2A-B**, raising the possibility of a potential functional link of BLTP3A to LRRK1 and LRRK2. However, given the inconsistency of these colocalizations this potential link was not further investigated in this study.

The association of BLTP3A with lysosomes is mediated by its N-terminal region where the Rab7 binding site is located

To confirm that Rab7 is responsible for the association of BLTP3A-positive vesicles with lysosomes (Gillingham et al., 2019), BLTP3A-mRFP was co-expressed in RPE-1 cells with either WT RAB7 (GFP-Rab7$_{WT}$) or dominant negative (DN) Rab7 (GFP-Rab7$_{T22N}$), i.e. a mutant Rab7 that sequesters its guanylnucleotide exchange factor (GEF) to prevent formation of GTP-loaded Rab7 (**Figure 2A**) (Stenmark and Olkkonen, 2001). The coexpression of WT Rab7, which localized along the entire surface of endolysosomes, but not within the vesicle clusters, did not alter the localization of BLTP3A-mRFP (**Figure 2A**). In contrast, coexpression of GFP-Rab7$_{T22N}$ abolished the association of BLTP3A-mRFP foci with lysosomes and induced the expansion of the BLTP3A foci free in the cytoplasm (**Figure 2A**), which CLEM confirmed to represent large accumulations of vesicles no longer associated with lysosomes (**Figure 2B**).

In order to determine the region of BLTP3A responsible for the association with Rab7, which could provide insight into the orientation of BLTP3A at the lysosome-vesicle interface, we generated chimeras of BLTP3A and BLTP3B using BLTP3B tagged with mRFP at its C terminus as a backbone (**Figure 2C**). As BLTP3B does not associate with Rab7 in spite of its close similarity to BLTP3A, we searched for a.a. sequences of BLTP3A which would confer Rab7 binding and lysosome localization to BLTP3B. A chimera ($BLTP3_{chimera\text{-}1}$) in which its first RBG module (a.a. 1-125, which includes the so-called chorein domain) was replaced by the first RBG module of BLTP3A (a.a 1-125) formed large clusters but such clusters were not associated with lysosomes (**Figure 2D**), as expected for BLTP3B. In contrast, a chimera ($BLTP3_{chimera\text{-}2}$) in which its second RBG module (a.a. 126-319) was replaced by the equivalent module of BLTP3A (a.a. 126-322) localized to LAMP1-GFP compartments similar to WT BLTP3A (**Figure 2D**), suggesting that the second RBG module of BLTP3A is sufficient for the Rab7-dependent lysosomal localization.

Moreover, a truncated construct comprising the first 2 RBG motifs of BLTP3A plus the first β-strand of the third RBG module of the same protein resulted in a fusion protein ($BLTP3A_{1\text{-}336}$-mRFP) that localized at lysosomes (**Figure 2D & 2E**), confirming the presence of the Rab7 binding site in this BLTP3A fragment. Notably, this fragment decorated homogenously the entire lysosomal surface, without forming the foci on their surface that reflect vesicle accumulations. These findings were further supported by the exogenous expression of Rab7 constructs. Expression of WT Rab7 greatly enhanced the localization of $BLTP3A_{1\text{-}336}$-mRFP around the entire lysosomal surface (**Figure 2F**), while the expression of dominant negative Rab7 (GFP-$Rab7_{T22N}$) resulted in a diffuse localization of $BLTP3A_{1\text{-}336}$-mRFP throughout the cytosol (**Figure 2F**). We conclude that a portion of BLTP3A near its N-terminus is necessary and sufficient for the localization of BLTP3A at lysosomes.

The C-terminal region of BLTP3A mediates its interaction with vesicles.

Rab7-dependent binding of BLTP3A to lysosomes via its N-terminal region implies that its C-terminal portion is likely responsible for vesicle binding and clustering (**Figure 2G**). To test this hypothesis, we generated BLTP3A constructs with C-terminal deletions and expressed them in cells also expressing dominant negative Rab7 (GFP-$Rab7_{T22N}$) to determine whether they could still cluster vesicles (**Figure 3A**). Deletion of the C-terminal helix of BLTP3A and of the linker that connects this helix to the last RBG motif ($BLTP3A_{1\text{-}1364}$-mRFP) did not affect the property of BLTP3A to cluster VAMP7-vesicles (detected by immunofluorescence using antibodies against VAMP7) similar to wild-type BLTP3A. However, a further truncation (construct $BLTP3A_{1\text{-}1327}$-mRFP) including the last two beta-strands of the sixth and final RBG motif of the channel, resulted in a protein that was diffusely cytosolic and did not cluster vesicles. The only accumulation of BLTP3A observed in these cells was a single cluster close to the nucleus (**Figure 3A**), most likely reflecting its interaction with Rab45 at the centrosomal area (**Supplemental Figure 1A**), but this cluster was VAMP7 negative, in agreement with the loss of vesicle binding (**Figure 3A**) Neither C-terminal truncation abolished localization to lysosomes (**Supplemental Figure 2C**). We conclude that the C-terminal portion of BLTP3A is necessary to interface with small vesicles.

321 We also attempted to identify BLTP3A binding partners on the vesicles. Towards this aim, we
322 carried out anti-V5 affinity purification from non-ionic detergent solubilized A549 cells where
323 BLTP3A was tagged at the endogenous locus, i.e. experimental conditions optimally suited to
324 reveal physiological binding partners (**Figure 3B**). Affinity-purified proteins were then identified
325 by mass spectrometry (**Figure 3C**). Unedited A549 cells were used as controls. This search did
326 not identify any obvious candidate binding protein. While two of the top specific hits, Rab27B and
327 its effector melanophilin (MLPH) are membrane associated proteins of transport vesicles (Nagata
328 et al., 1990; Ménasché et al., 2000; Hume et al., 2001; Bahadoran et al., 2001; Nagashima et al.,
329 2002; Strom et al., 2002), we failed to obtain evidence for a concentration of these proteins on
330 BLTP3A-positve vesicles. Thus these two proteins were not further studied in the context of the
331 present study. Two other top hits, however, the two mATG8 family members GABARAP and
332 MAP1LC3B, provided insight into properties of BLTP3A which will be discussed below.
333
334 **Lysosomal damage disrupts the Rab7-dependent association of BLTP3A positive vesicles**
335 **with lysosomes**
336
337 Perturbation of the membranes of lysosomes, for example by L-Leucyl-L-Leucine methyl ester
338 (LLOMe), a dipeptide taken-up into lysosomes where it is metabolized into membranolytic
339 peptides (Goldman and Kaplan, 1973; Thiele and Lipsky, 1990; Uchimoto et al., 1999), was
340 reported to trigger the rapid recruitment of factors to their surface that may help prevent or repair
341 damage (Skowyra et al., 2018; Radulovic et al., 2018; Shukla et al., 2022; Herbst et al., 2020;
342 Radulovic et al., 2022; Tan and Finkel, 2022; Bentley-DeSousa and Ferguson, 2023; Wang et al.,
343 2024a). These include, besides ESCRT components, shuttle-like lipid transfer proteins such as
344 ORP family members (Tan and Finkel, 2022; Radulovic et al., 2022) and bridge-like lipid transfer
345 proteins structurally related to BLTP3A (Wong et al., 2019; Neuman et al., 2022) such as VPS13C
346 (Wang et al., 2024a) and ATG2 (Tan and Finkel, 2022; Cross et al., 2023). Both VPS13C and
347 ATG2 are thought to mediate bulk phospholipid delivery to damaged lysosomes from the ER,
348 which they bind via their N-terminal chorein domain (Kumar et al., 2018; Valverde et al., 2019;
349 Osawa et al., 2019; Maeda et al., 2019; Wang et al., 2024a).
350
351 Although a pool of BLTP3A is already at contacts with lysosomes under control conditions (but in
352 an opposite orientation relative to that of the ATG2 and VPS13C at contacts of the ER with
353 damaged lysosomes, i.e. with its N-terminal chorein domain facing the lysosomal membrane), we
354 explored whether LLOMe dependent damage of lysosomes had an impact on BLTP3A
355 localization in RPE-1 cells. Surprisingly, and in contrast to the damage-dependent recruitment of
356 VPS13C (Wang et al., 2024a) and ATG2 (Tan and Finkel, 2022) to lysosomes, the focal
357 accumulations of BLTP3A on lysosomes, which reflect accumulations of BLTP3A-positive
358 vesicles, dissociated within minutes from the lysosomal surface upon its damage (**Figure 4A**),
359 whose occurrence was confirmed by the recruitment of cytosolic IST1 (mApple-IST1) (**Figure**
360 **4A**), an ESCRT-III subunit (Skowyra et al., 2018; Corkery et al., 2024). This LLOMe-dependent
361 dissociation of BLTP3A positive vesicle clusters from lysosomes, however, was not accompanied
362 by a dispersion of the vesicle clusters themselves, indicating that the Rab7-dependent interaction
363 of BLTP3A with lysosomes, not the interactions of BLTP3A which bind and clusters vesicles, was
364 perturbed. This was confirmed by the finding that the Rab7 binding N-terminal fragment of

365 BLTP3A (BLTP3A$_{1-336}$-mRFP), which does not bind vesicles, dissociated from lysosomes,
366 visualized in this experiment by the lysosomal protein NPC1 (NPC1-GFP) (**Figure 4B**).
367 Mechanisms responsible for the dissociation of BLTP3A from lysosomes remain unknown.
368 BLTP3A dissociation was not due to loss of Rab7 binding sites on lysosomes as the binding of
369 VPS13C, which is recruited to lysosomes with a kinetic similar to that of BLTP3A dissociation,
370 requires active Rab7 at these organelles (Wang et al., 2024a). Likewise dissociation was not due
371 to the rapid phosphorylation of Rab7 at serine 72, a process primarily mediated by the kinase
372 activity of LRRK1 (Wang et al., 2024a) with an additional variable contribution of the kinase TBK1
373 (Nirujogi et al., 2021; Fujita et al., 2022; Heo et al., 2018; Talaia et al., 2024), as over-expression
374 of a dominant-protein kinase active LRRK1 mutant (GFP-LRRK1^{K746G}) did not affect the
375 localization of BLTP3A-mRFP foci next to lysosomes in RPE-1 cells (**Supplemental Figure 1F &**
376 **Supplemental Figure 1H**).
377
378 **CASM-dependent reassociation of BLTP3A with the lysosomal membrane after its LLOMe**
379 **induced rapid dissociation**
380
381 One event triggered by LLOMe-dependent damage of the lysosomal membrane is activation of
382 CASM (Conjugation of Atg8 to Single Membranes) (Durgan and Florey, 2022; Boyle et al., 2023;
383 Corkery et al., 2023; Kaur et al., 2023; Fischer et al., 2020). This is the process whereby lysosome
384 perturbations that drive V-ATPase V0-V1 association in their membrane to enhance its proton
385 pump activity also result in the recruitment of a subset of components of the classical autophagy
386 pathway resulting in the lipidation and recruitment to the lysosomal membrane of mATG8 family
387 proteins. These are small adaptors that are recruited to membranes in response to their triggered
388 conjugation to PE or PS and bind proteins which contain the so-called LC3-interacting region
389 (LIR) motif, typically found in disordered protein regions. Atg8 family proteins, which comprise six
390 members in mammals, are well established players in conventional autophagy (Melia et al., 2020;
391 Nieto-Torres et al., 2021; Figueras-Novoa et al., 2024; Deretic et al., 2024): they interact with the
392 isolation membrane via their lipid tail and recruit cargo targeted for autophagy via their LIR-motif-
393 dependent interactions. However, the discovery of CASM has now revealed another important
394 role of these proteins which is being intensely investigated (Durgan and Florey, 2022).
395
396 In view of the identification of two mATG8 proteins, MAP1LC3B and GABARAP, as interactors of
397 BLTP3A (**Figure 3C**), we further explored a potential role of CASM in BLTP3A dynamics. A search
398 for LIR motifs in BLTP3A using the publicly available iLR Autophagy Database
399 (https://ilir.warwick.ac.uk/index.php) predicts such a motif [Position Specific Scoring Matrix
400 (PSSM) score: 16] within a disordered loop projecting out from the C-terminal region of BLTP3A,
401 but not of BLTP3B, from several mammalian species, including humans (aa 1129-1134) (**Figure**
402 **5A**) (see also (Tu and Brumell, 2020)). The high degree of conservation of this motif relative to its
403 surrounding a.a. sequences suggests its physiological importance, consistent with our co-affinity
404 purification results. Moreover, structure-prediction algorithms (Abramson et al., 2024) predict with
405 high confidence an interaction between the LIR motif of BLTP3A and the majority of the six known
406 mATG8 proteins (**Supplemental Figure 2D & 2E**).
407

To determine a potential physiological role of an mATG8-BLTP3A interaction, we co-expressed BLTP3A-mRFP and GFP-LC3B in RPE-1 cells. The localization of BLTP3A-mRFP on lysosomes and to large accumulations was not changed by the over-expression of GFP-LC3B, which was mostly cytosolic (**Figure 5B**). Starvation of these cells resulted in the formation of GFP-LC3B-positive foci, as expected, but did not alter the localization of BLTP3A-mRFP, indicating that BLTP3A does not play a role in conventional autophagy (**Figure 5B**).

We next monitored the response of LC3B relative to BLTP3A after addition of LLOMe. In the first few minutes after LLOMe addition, when BLTP3A-mRFP clusters as described above dissociated from lysosomes, GFP-LC3B fluorescence remained cytosolic with no overlap with the BLTP3A fluorescence (**Figure 5C**). After ~5-10 mins of LLOMe treatment, however, GFP-LC3B began to accumulate on the surface of some lysosomes (**Figure 5C**), as previously reported (Cross et al., 2023), and this association correlated with the reassociation of a pool of BLTP3A-mRFP to such lysosomes, consistent with BLTP3A being an mATG8 effector. This BLTP3A pool colocalized with LC3 along the entire surface of lysosomes and did not occur in focal accumulations indicating that it did not reflect presence of large vesicle clusters, although large BLTP3A positive larger clusters persisted in the surrounding cytoplasm (**Figure 4A & Figure 5C**). Similar results were observed upon addition of the lysosome stressor glycyl-L-phenylalanine 2-naphthylamide (GPN) (**Supplemental Figure 3A**) (Chen et al., 2024; Durgan and Florey, 2022), another CASM activator. Deletion of the LIR motif of BLTP3A (BLTP3AΔLIR-mRFP) did not affect the localization of BLTP3A in the absence of LLOMe treatment and did not abolish the shedding of BLTP3A clusters upon LLOMe treatment but abolished its recruitment to GFP-LC3B positive lysosomes after LLOMe (**Figure 5D**), demonstrating that the LIR motif of BLTP3A is necessary for such recruitment. These observations were further validated by CLEM and correlative fluorescence-focused ion beam scanning electron microscopy (FIB-SEM), which allowed us to obtain views of the entire surface of lysosomes in RPE-1 cells positive for exogenous BLTP3A-mRFP and GFP-LC3B after 15 mins of LLOMe exposure (**Figure 5E**). While vesicles were observed on LC3-positive lysosomes, their abundance did not correlate with the presence of LC3 and BLTP3A along the entire lysosome surface (**Figure 5E & Supplemental Figure 3B)**. Importantly, correlative fluorescence-FIB-SEM microscopy also showed abundant presence of ER contacts (**Figure 5E**), as expected after LLOMe treatment (Tan and Finkel, 2022; Radulovic et al., 2022; Wang et al., 2024a).

Collectively, these results suggest that the orientation of BLTP3A mediated by its LIR domain at the lysosome surface is not the same as the one mediated by Rab7 (**Figure 5F**). The binding mediated by the LIR domain would leave the N-terminal chorein domain region of BLTP3A available for binding to the ER to allow a flux of phospholipids from the ER to lysosomes as in the case of VPS13C and ATG2. These findings raise the possibility that BLTP3A may cooperate with VPS13C and ATG2 in delivering lipids to lysosomal membrane after its damage.

The loss of BLTP3A in A549 cells enhances lysosome fragility

To directly test whether BLTP3A plays a role in counteracting the damaging effect of LLOMe, we performed experiments in BLTP3A KO cells. The BLTP3A gene was edited in A549 cells to

include frameshift mutations in exon 2 (**Supplemental Figure 3C**) and absence of the BLTP3A protein in lysates from these cells was confirmed by western blotting (**Figure 6A**). Interestingly, while levels of some proteins of the late endosomal system, for example Rab7, were unchanged in the lysates of KO cells relative to controls, a ~5-fold decrease in the protein levels of LAMP1 was observed (**Figure 6A & Supplemental Figure 3D)**, confirmed by a decrease of anti-LAMP1 immunofluorescence, despite no obvious difference in lysosome number (**Figure 6B**), pointing to an important role of BLTP3A in lysosome homeostasis.

To assess lysosome damage, we used the galectin-3 (Gal3)-based immunofluorescence assay (**Figure 6C**). Gal3, which is normally diffuse in the cytosol, binds to β-galactosides and accumulates within lysosomes only when the membrane of these organelles is damaged. This accumulation results in bright puncta of anti-Gal3 immunofluorescence which corresponds to lysed lysosomes. Upon addition of LLOMe to A549 cells, bright puncta of Gal3 immunoreactivity started to appear in both wild-type and BLTP3A KO cells, (**Figure 6C**). However, at the 30 and 60 min timepoints, a higher number of Gal3 spots were observed in BLTP3A KO cells relative to wild-type cells (**Figure 6D**) revealing a greater fragility of KO cells.

DISCUSSION

Our study shows that BLTP3A, a protein expected to transfer lipids between adjacent membranes via a bridge-like mechanism, is a component of protein networks implicated in membrane traffic in late endosomes/lysosomes and that lysosome damage has an impact on its localization. BLTP3A binds and cluster vesicles of the endocytic system positive for VAMP7 and VAMP4 and tether them to lysosomes via an interaction of its N-terminal region with lysosome-bound Rab7. Upon lysosome membrane damage and the subsequent recruitment to their surface of mATG8 family proteins via CASM, this Rab7-dependent interaction is lost. However, within minutes, BLTP3A then reassociates with damaged lysosomes by interacting with mATG8 proteins via a LIR motif present in a long predicted unfolded loop emerging form the C-terminal region of the protein. As we discuss below, we suggest that this second interaction is the one relevant for bridge-dependent lipid transfer, and that BLTP3A may cooperate with other BLTPs in the response of cells to lysosome damage. Accordingly, we have found evidence for an increased fragility of lysosomes in response to damage in BLTP3A KO cells.

The property of BLTP3A to associate with small vesicles and induce their striking accumulation when overexpressed is shared with BLTP3B (Hanna et al., 2022). Moreover, BLTP3A- and BLTP3B-positive vesicles have similar size, share at least one cargo, ATG9A, and clusters of them are closely associated to other organelles. However, these organelles differ for the two proteins: Rab5 positive early endosomes in the case of BLTP3B and Rab7 positive lysosomes in the case of BLTP3A. Moreover, BLTP3A and BLTP3B positive vesicles differ at least partially in protein composition, as only BLTP3A positive clusters are strongly immunolabeled by antibodies directed against VAMP7 and VAMP4.

Both VAMP7 and VAMP4 were reported to directly bind via their longin domain to a small N-terminal motif present within the Parkinson's disease protein LRRK2 and its paralogue LRRK1

496 (Wang et al., 2018; Filippini et al., 2023). It was therefore of interest that in some cells a striking
497 colocalization was observed between either GFP-LRRK1 or GFP-LRRK2 (exogenous and thus
498 overexpressed proteins) with vesicle clusters induced by BLTP3A overexpression, although why
499 such a striking colocalization was observed only in a subset of cells remains unclear. Evidence
500 that both LRRK1 and LRRK2 have a role in lysosome biology makes a potential functional link
501 between them and BLTP3A plausible. Interestingly, proteomics studies of the impact of LRRK2
502 kinase activity on protein levels in lungs have identified among major alterations changes in the
503 levels of Rab27A, Rab27B, melanophilin, and Rab45 (Suppl Fig. 1A and Fig. 3C) (D. Alessi,
504 Dundee, UK, personal communication) proteins that our present study has linked to BLTP3A
505 biology, although mechanistic aspects remain to be elucidated.
506
507 BLTP3 vesicle clusters are reminiscent of the clusters of synaptic vesicles at synapses. Such
508 clusters were shown to have the properties of liquid biomolecular condensates (Milovanovic and
509 De Camilli, 2017; Milovanovic et al., 2018; Park et al., 2021). Similarly, vesicle clusters involving
510 BLTP3A and BLTP3B are very dynamic (see for example movies of these clusters in (Hanna et
511 al., 2022)). The assembly of BLTP3A-positive vesicle clusters and their anchorage to
512 endosomes/lysosomes, implies a minimum of three direct or indirect interactions of BLTP3A: 1)
513 an interaction with vesicles, 2) an interaction with itself or with adaptor proteins to cluster vesicles
514 and 3) an interaction with lysosomes to account for the anchoring of the vesicle clusters to these
515 organelles.
516
517 We have shown that the interaction with lysosomes of vesicle-associated BLTP3A (interaction
518 #3) is mediated by the binding to lysosome-bound Rab7, consistent with its being a Rab7 effector.
519 Moreover, our results suggest that such an interaction involves the N-terminal region of BLTP3A,
520 where we have detected the Rab7 binding site. We have also shown that the binding to vesicles
521 (interaction #1) is mediated by the opposite end of the protein, i.e. its C-terminal region, but so
522 far, we have not detected a binding partner. We note that even in the case of synaptic vesicle
523 condensates (Milovanovic et al., 2018; Park et al., 2021), which involve interactions between
524 synapsin (a cytosolic protein) (Südhof et al., 1989; De Camilli et al., 1990), and synaptophysin (a
525 vesicle protein) (Johnston et al., 1989), a direct interaction between the two proteins could not be
526 detected by co-precipitation (Park et al., 2021), although clearly such an interaction occurs in
527 living cells where low affinity is counteracted by multivalency: a multiplicity of low affinity
528 interactions between synapsin with itself and with synaptophysin, a protein present in multiple
529 copies on the vesicles.
530
531 Concerning the mechanisms responsible for vesicle clustering (interaction #2), these may involve
532 self-association of BLTP3A via low complexity unfolded sequences that project out of its rod-like
533 core, or binding of BLTP3A to yet to be discovered adaptor/crosslinker proteins. As the property
534 to cluster vesicles is shared by both BLTP3A and BLTP3B, such a property must rely on shared
535 molecular determinants of these two proteins. Ongoing work is addressing these mechanisms.
536 The property of BLTP3 proteins to cluster vesicles into small packages may be an important
537 aspect of their physiological function as BLTP3B-positive vesicles were shown to be organized in
538 small clusters even at physiological levels of expression (Hanna et al., 2022). Large clusters likely
539 result from BLTP3 overexpression, although other scenarios, such as that BLTP3 overexpression

may result in vesicle accumulation due to a dominant negative effect on their fusion with downstream targets, cannot be ruled out.

Our study indicates that the Rab7-dependent association of BLTP3A with lysosomes requires a portion of BLTP3A located in proximity of its N-terminal region, the so-called chorein motif (Kumar et al., 2018). In most other BLTP family members, the chorein or chorein-like motifs are localized at the ER, which is typically thought to be the “donor” membrane in their lipid transfer function (Kumar et al., 2018; Valverde et al., 2019; Guillén-Samander et al., 2021; Cai et al., 2022b; Levine, 2019; Osawa et al., 2019). This is also the case for the other two BLTPs reported to be implicated in ER to lysosomes lipid flux, VPS13C (Kumar et al., 2018; Wang et al., 2024a) and ATG2 (Tan and Finkel, 2022; Cross et al., 2023). Thus, we consider it unlikely that the orientation of BLTP3A when cross-linking vesicles to Rab7 may be relevant to its lipid transfer properties. Potential insight about a condition where a bridge-like lipid transfer function of BLTP3A may be fulfilled came from analysis of the response of BLTP3A to lysosome damage.

Lysosomal membrane damage activates multiple response mechanisms at timepoints ranging from seconds to hours (Skowyra et al., 2018; Radulovic et al., 2018; Tan and Finkel, 2022; Meyer and Kravic, 2024; Wang et al., 2024a). Conjugation of mATG8 proteins to the surface of lysosomes (CASM pathway) is one such response (Durgan and Florey, 2022). mATG8 proteins can be detected on lysosomes ~5-10 mins after the initiation of membrane damage, similar to the time frame of BLTP3A reassociation. It is therefore of great interest that 1) top hits identified from our immunoprecipitation of endogenously tagged BLTP3A^V5 from A549 cells are two mATG8 proteins (MAP1LC3B and GABARAP) and 2) BLTP3A contains a LIR motif (i.e. an Atg8 binding consensus) within a disordered loop projecting out of the C-terminal rod-like region. Accordingly, we found that the reassociation of BLTP3A after LLOMe follows the accumulation of LC3B on the surface of lysosomes and that the LIR motif is required for the reassociation of BLTP3A with their surface.

The LIR motif of BLTP3A is localized on a long (305 a.a.) predicted unfolded loop emerging from the C-terminal portion of BLTP3A, which is the portion of the protein expected to bind vesicles. However, the bulk of the pool of BLTP3A that reassociates with the lysosomal surface is not bound to small vesicles, although clusters of BLTP3A positive vesicles persist in the cytoplasm, suggesting that the LIR motif-dependent interaction of BLTP3A with lysosome-bound LC3B is mutually exclusive with its association with vesicles, possibly because of steric hindrance or regulatory mechanisms. A binding of BLTP3A to lysosomes via its LIR motif, rather than by Rab7, would leave its N-terminal chorein domain region, no longer engaged by Rab7, free to interact with the ER (**Figure 5F**).

Lysosome membrane damage is known to result in the formation of ER-lysosome tethers comprising other lipid transfer proteins, such as ORP proteins (Tan and Finkel, 2022; Radulovic et al., 2022), VPS13C (Wang et al., 2024a) and ATG2 (Tan and Finkel, 2022; Cross et al., 2023), most likely as a cellular response aimed at protecting or repairing membranes by delivering new lipids. This is consistent with the abundant presence of ER-lysosome contacts that we have observed in 3D volumes of lysosomes of RPE1 cells exposed to 15 min LLOMe. We suggest that

584 under these conditions, close appositions between lysosomes and the ER facilitate an interaction
585 of the chorein domain of BLTP3A with the ER, thus allowing the formation of BLTP3A-dependent
586 ER-to-lysosome bridges that may cooperate with other BLTPs in delivering membrane lipids from
587 the ER to lysosomes. In support of such an idea, we found increased lysosome fragility (indicated
588 by Gal3 puncta) in A549 cells that lack BLTP3A in comparison to wild-type after ≥30 mins LLOMe
589 treatment. How delivery of new membrane lipids helps prevent or repair damage of the lysosome
590 membrane remain unclear, but a cooperation with ESCRT complexes, which are also rapidly
591 recruited to lysosome in response to damage, is likely (Skowyra et al., 2018; Radulovic et al.,
592 2018).
593
594 In conclusion, our study links BLTP3A to the function of late endosomes and lysosomes and
595 suggests that one of its functions is to cooperate in the response to lysosome damage as an
596 effector of CASM. As lysosomes play a key role in cells of the immune system, it is of special
597 interest that several coding variants of BLTP3A are associated with susceptibility to systemic
598 lupus erythematosus (SLE) (Gateva et al., 2009; Zhang et al., 2011; Wen et al., 2020), a chronic
599 autoimmune disease.
600

601 MATERIALS AND METHODS

602

603 Antibodies and Reagents

604
605 The list of plasmids, antibodies, their working dilution, and the supplier for this study can be
606 found in the **Key Resource Table** at the following link:
607 https://docs.google.com/spreadsheets/d/1RVOPrz9L_QFf1PetDbkS3vPMHXVXI_QYCKIUzjgA3
608 lc/edit?usp=sharing
609

610 Generation of Plasmids

611
612 All BLTP3A and BLTP3B ORFs used in this study utilized a human codon optimized sequence
613 designed and purchased from Genscript. Codon optimized human BLTP3 chimeras were
614 amplified using PCR from the pcDNA3.1 plasmid and ligated into a pmCh-N1 plasmid. Most
615 constructs were generated with regular cloning protocols or through site-directed mutagenesis.
616 The desired ORFs were amplified by PCR and inserted into plasmids through enzyme digestions
617 and ligation. Some amplified ORFs were ligated using HiFi assembly (NEB). Details of primer
618 sets, enzymes, techniques, and plasmids used for each construct can be found in the **Key**
619 **Resource Table**.
620
621 Detailed protocol for the molecular cloning of BLTP3 plasmids for expression in mammalian cells
622 is at: https://dx.doi.org/10.17504/protocols.io.8epv5z5kjv1b/v1
623

624 Correlative Light and Electron Microscopy

625
626 For TEM CLEM, RPE-1 cells were plated on 35 mm gridded, glass-bottom MatTek dish (P35G-
627 1.5-14-CGRD) and transfected as described above with BLTP3A-mRFP, LAMP1-GFP, mito-BFP.

628 Cells were pre-fixed in 4% PFA in dPBS then washed with dPBS before fluorescence light
629 microscopy imaging. Regions of interest were selected and their coordinates on the dish were
630 identified using phase contrast. Cells were further fixed with 2.5% glutaraldehyde in 0.1 M sodium
631 cacodylate buffer, postfixed in 2% OsO_4 and 1.5% $K_4Fe(CN)_6$ (Sigma-Aldrich) in 0.1 M sodium
632 cacodylate buffer, *en bloc* stained with 2% aqueous uranyl acetate, dehydrated in graded series
633 of ethanols (50%, 75%, and 100%), and embedded in Embed 812. Cells of interest were relocated
634 based on the pre-recorded coordinates. Ultrathin sections (50-60 nm) were post-stained with
635 uranyl acetate substitute (UranyLess, EMS), followed by a lead citrate solution. Sections were
636 observed in a Talos L 120C TEM microscope at 80 kV, images were taken with Velox software
637 and a 4k × 4K Ceta CMOS Camera (Thermo Fisher Scientific). Except noted all reagents were
638 from EMS (Electron Microscopy Sciences), Hatfield, PA.
639
640 Detailed protocol for 2D TEM CLEM is at:
641 https://dx.doi.org/10.17504/protocols.io.261gend2jg47/v1
642
643 **FIB-SEM Sample Preparation and Imaging**
644
645 One Epon-embedded sample of RPE-1 cells expressing BLTP3A-mRFP and GFP-LC3B after 15
646 mins of LLOMe exposure, was mounted onto the top of a 1 mm copper stud using Durcupan,
647 ensuring optimal charge dissipation by maintaining contact between the heavy metal-stained
648 sample and the copper stud. The vertical sample post was then trimmed to a small block
649 containing the Region of Interest (ROI), with dimensions of 80 μm² in width (perpendicular to the
650 ion beam) and 75 μm² in depth (in the ion beam direction). Precise ROI targeting and trimming
651 were achieved using overlay images from light fluorescence microscopy and X-ray tomography
652 data acquired with a Zeiss Versa XRM-620. The detail approach was previously described by
653 (Pang and Xu, 2023). To enhance conductivity, thin layers of conductive material—10 nm of gold
654 followed by 40 nm of carbon—were deposited onto the trimmed sample using a Leica EM ACE600
655 coater.
656
657 The FIB-SEM prepared sample was imaged using a customized enhanced FIB-SEM microscope
658 (Xu et al., 2017, 2021). The images were acquired using a 500 pA current SEM probe at 0.7 keV.
659 The scan rate was 400 kHz, with a 2-nm pixel along x and y axes. A 2-nm z-step was achieved
660 by ~5 seconds of milling with a 15-nA Ga^+ beam at 30 kV. A total volume of 12 × 6 × 12 μm^3 was
661 acquired over 8 days at a rate of 1 minute per frame. The raw image stack was aligned using a
662 SIFT based MATLAB script and binned 2-to-1 along x, y, and z axes to create a final dataset with
663 4 × 4 × 4 nm^3 voxels, which can be viewed in any arbitrary orientations.
664
665 **Cell culture and Transfections**
666
667 hTERT-RPE-1 cells were a kind gift of A. Audhya (University of Wisconsin, Madison, WI). A549
668 and COS-7 cells were obtained from ATCC. All mammalian cells were maintained at 37ºC in
669 humidified atmosphere at 5% CO_2 unless noted otherwise. A549 and COS-7 cells were grown in
670 DMEM and RPE-1 cells in DMEM/F12 medium (Thermo Fisher Scientific) supplemented with 10%
671 FBS, 100 U/mL penicillin, 100mg/mL streptomycin. 2mM glutamax (Thermo Fisher Scientific) was

672 added to all media for RPE-1 cells. All cell lines were routinely tested and always resulted free
673 from mycoplasma contamination.
674
675 Transient transfections were carried out on cells that were seeded at last 8 h prior. All
676 transfections of plasmids used FuGENEHD (Promega) to manufacturers specifications for 16-24
677 h in complete media without antibiotics.
678
679 Detailed protocol for cell culture, transfection, immunocytochemistry, and imaging:
680 https://dx.doi.org/10.17504/protocols.io.eq2lyp55mlx9/v1
681
682 **Immunoblotting and Imaging Procedure**
683
684 All cell samples analyzed by immunoblotting were scraped from plates and harvested by
685 centrifugation (500xg for 5 minutes). The pellet was washed with ice-cold dPBS and centrifuged
686 again in a 1.7mL Eppendorf tube. The cell pellet was resuspended in Lysis buffer (20mM Tris-
687 HCl pH 7.5, 150mM NaCl, 1% SDS, 1mM EDTA) containing protease inhibitor cocktail (Roche).
688 The lysate was clarified by centrifugation (17,000xg for 10 minutes) and a small portion of lysate
689 was reserved for quantification of protein concentration by Bradford. The remaining lysate was
690 then mixed with 5x SDS sample buffer (Cold Spring Harbor) to 1x concentration and then heated
691 to 95°C for 3 minutes. 15-25ug of protein samples were separated by electrophoresis on a 4-20%
692 Mini-PROTEAN TGX gel and then subjected to standard western blot transfer and procedures.
693 Blots were imaged using the Odyssey imaging system (LI-COR) using manufacturers protocols.
694 All primary antibodies used in this study are listed in the **Key Resource Table**.
695
696 **Mouse Tissue Lysate Preparation**
697
698 Tissues were collected from sacrificed WT C57BL/6J mice (Jackson Laboratory strain #000664).
699 For each 1 g of material, 10 ml of buffer (25 mM Hepes, pH 7.4, 200 mM NaCl, 5% glycerol,
700 protease inhibitors) was added. Mechanical lysis was performed using a glass dounce-
701 homogenizer (15 strokes). Triton X-100 was added to 1%, and material was rotated at 4°C for 30
702 min. Material was centrifuged at 1,000 g to remove cell debris and the collected supernatant was
703 centrifuged at 27,000 g for 20 min. The resulting supernatant mixed was flash frozen and stored
704 at −80°C until use.
705
706 **Live Cell Imaging and Immunofluorescence**
707
708 For all live cell microscopy cells were seeded on glass-bottom mat-tek dishes (MATtek
709 corporation) 5500/cm^2 in complete media. Transfections were carried out as described above.
710 Spinning-disk confocal imaging was preformed 16-24 h post transfection using an Andor
711 Dragonfly 200 (Oxford Instruments) inverted microscope equipped with a Zyla cMOS 5.5 camera
712 and controlled by Fusion (Oxford Instruments) software. Laser lines used: DAPI, 440nm; GFP,
713 488; RFP, 561; Cy5, 647. Images were acquired with a PlanApo objective (60x 1.45-NA). During
714 imaging, cells were maintained in Live Cell Imaging buffer (Life Technologies) in a cage incubator
715 (Okolab) with humidified atmosphere at 37°C. LLOMe (Sigma-Aldrich, CAS: 1668914-8) and GPN

716 (Cayman Chemical, CAS: 14634) were dissolved in ethanol and used at a final concentration of
717 1 mM for all imaging experiments. All live imaging experiments are representative of at least 10
718 independent repeats.
719
720 Immunofluorescent experiments were performed with cells grown on #1.5 glass cover slips. Cells
721 were fixed with 4% PFA in PBS (Gibco, 14190144) for 15 mins at room temperature, washed 3x
722 with PBS, permeabilized using antibody dilution buffer (1x PBS containing 0.2% saponin and 2%
723 BSA) at 4°C overnight with the indicated primary antibodies. Slides were washed three times with
724 PBS containing 0.02% saponin to remove excess primary antibody and subsequently incubated
725 with secondary antibodies diluted in antibody dilution buffer for 45 min at room temperature in the
726 dark. Slides were washed again three times to remove secondary antibody with PBS containing
727 0.02% saponin prior to mounting.
728
729 **Lysosomotropic drug treatments**
730
731 Cells (RPE-1 or A549) were seeded 16-24 hrs before treatments. A fresh 333mM stock solution
732 of LLOMe in ethanol was prepared and kept on ice. For live-imaging experiments, a 2x stock of
733 LLOMe or GPN (2 mM) was prepared in complete media immediately before adding to an equal
734 volume of complete media on a Mattek dish. Cells were imaging at 37C with 5% CO2 at all times.
735 For lysosome damage experiments (galectin-3 immunofluorescence), LLOMe (1 mM) was added
736 to complete medium pre-warmed to 37C and immediately added to cells. Cells were then
737 incubated at 37C with 5% CO2 for 15, 30, or 60 minutes. Untreated cells received an identical
738 volume of vehicle (ethanol) in complete medium for 15 minutes and served as a baseline. After
739 incubation with LLOMe or vehicle, cells were fixed as described above before being incubated
740 overnight at 4C with antibodies against galectin-3.
741
742 **Quantification of Gal3 puncta in A549 cells**
743
744 Cell boundaries were drawn by hand in Fiji. Minimum and maximum display values of 3000 and
745 8000 were used to detect fluorescence. Remaining background signal after setting these
746 minimum and maximum display values was smoothened using the “Mean” filter in Fiji set to a
747 radius of 2 pixels. After smoothening, Fiji’s default thresholding algorithm was used to identify the
748 foreground objects and create a mask of Gal3 spots. The resulting mask was processed using
749 Fiji’s binary “Watershed” separation technique to separate foreground objects (Gal3 spots) that
750 were touching. Finally, using Fiji’s “Analyze particles” function, ROIs were generated for all mask
751 objects and counted as individual Gal3 spots. ROIs smaller than 3 pixels were considered noise
752 and were not included in the count.
753
754 **Generation of CRISPR Edited Cell Lines**
755
756 Endogenous tagging of A549 cells was carried out using a CRISPR/Cas9 ribonucleoprotein
757 (RNP) complex. Commercially purified Cas9 nuclease (IDT) was combined and incubated with
758 trans-activating CRISPR RNA (tracrRNA) and a BLTP3A-targeting guide RNA to form the RNP
759 complex. The RNP complex was then incubated with a single-stranded repair template containing
760 the insert sequence and ultimately delivered to A549 cells via electroporation. Subsequently, the
761 RNP-transfected pools were serially diluted and plated at 1 cell per well on a glass bottom 96-

762 well plate. Wells were expanded and tested for editing via PCR until an appropriate number of
763 edited clones were obtained. All gRNAs used in this study are listed in the **Key Resource Table**.
764
765 **Immunoprecipitation of Endogenously Tagged BLTP3A**
766
767 Wild-type or endogenously edited A549 cells expressing BLTP3A^V5 were grown to 90%
768 confluency on 15 cm plates (Falcon). Two 15 cm plates were used for each independent replicate
769 of wild-type and edited cells (n=3). Cells were washed with dPBS (Gibco) and then scrapped from
770 the surface of the plates into 2 mL of dPBS per plate. Cells were pelleted at 1000g for 5 min and
771 the dPBS supernatant was removed. Cells were resuspended in 2 mL of ice-cold lysis buffer (50
772 mM Tris pH 7.6, 150 mM NaCl, 1% Triton X-100, protease inhibitors [Roche]) and rotated at 4°C
773 for 20 mins. Cell lysates were spun at 17000g for 10 mins to clear insoluble material. The
774 supernatants were then added to 75 uL (slurry) of anti-V5 magnetic resin (ChromoTek) and let
775 rotate at 4°C for 2 hrs. Resin was washed twice for 5 mins rotating with ice cold lysis buffer and
776 then washed a third time without detergent for 5 mins (50 mM Tris pH 7.6, 150 mM NaCl, protease
777 inhibitors). Supernatant was removed and resin was stored at −80°C.
778
779 **Protein digestion**
780
781 The beads were resuspended in 80 µL of 2M Urea, 50 mM ammonium bicarbonate (ABC) and
782 treated with DL-dithiothreitol (DTT) (final concentration 1 mM) for 30 minutes at 37°C with shaking
783 at 1100 rpm on a Thermomixer (Thermo Fisher). Free cysteine residues were alkylated with 2-
784 iodoacetamide (IAA) (final concentration 3.67 mM) for 45 minutes at 25°C with shaking at 1100
785 rpm in the dark. The reaction was quenched using DTT (final concentration 3.67 mM), and LysC
786 (750 ng) was added, followed by incubation for 1h at 37°C at 1150 rpm. Finally, trypsin (750 ng)
787 was added, and the mixture was incubated for 16 hours at 37°C with shaking at 1150 rpm.
788
789 After incubation, an additional 500 ng of trypsin was added to the sample, followed by a 2-hour
790 incubation at 37°C at 1150 rpm. The digest was then acidified to pH <3 by adding 50%
791 trifluoroacetic acid (TFA), and the peptides were desalted on C18 stage tips (Empore C18
792 extraction disks). Briefly, the stage tips were conditioned with sequential additions of: i) 100 µL
793 methanol), ii) 100 µL 70% acetonitrile (ACN)/0.1% TFA, iii) 100 mL 0.1% TFA twice. After
794 conditioning, the acidified peptide digest was loaded onto the stage tip, and the stationary phase
795 was washed with 100 µL 0.1% formic acid (FA) twice. Finally, the peptides were eluted with 50
796 µL 70% ACN/0.1% FA twice. Eluted peptides were dried under vacuum in a Speed-Vac
797 centrifuge, reconstituted in 12 µL of 0.1% FA, sonicated and transferred to an autosampler vial.
798 Peptide yield was quantified using a NanoDrop (Thermo Fisher).
799
800 **Mass spectrometry analyses**
801
802 Peptides were separated on a 25 cm column with a 75 µm diameter and 1.7 µm particle size,
803 composed of C18 stationary phase (IonOpticks Aurora 3 1801220) using a gradient from 2% to
804 35% Buffer B over 90 minutes, followed by an increase to 95% Buffer B for 7 minutes (Buffer A:

0.1% FA in HPLC-grade water; Buffer B: 99.9% ACN, 0.1% FA) with a flow rate of 300 nL/min on a NanoElute2 system (Bruker).

MS data were acquired on a TimsTOF HT (Bruker) with a Captive Spray source (Bruker) using a data-independent acquisition PASEF method (dia-PASEF). The mass range was set from 100 to 1700 *m/z*, and the ion mobility range from 0.60 V.s/cm^2 (collision energy 20 eV) to 1.6 V.s/cm^2 (collision energy 59 eV), a ramp time of 100 ms, and an accumulation time of 100 ms. The dia-PASEF settings included a mass range of 400.0 to 1201.0 Da, mobility range 0.60-1.60, and an estimated cycle time of 1.80 seconds. The dia-PASEF windows were set with a mass width of 26.00 Da, mass overlap 1.00 Da, and 32 mass steps per cycle.

DIA data analysis

Raw data files were processed using Spectronaut version 17.4 (Biognosys) and searched with the PULSAR search engine against the Homo sapiens UniProt protein database (226,953 entries, downloaded on 2022/09/23). Cysteine carbamidomethylation was set as fixed modifications, while methionine oxidation, acetylation of the protein N-terminus, and deamidation (NQ) were defined as variable modifications. A maximum of two trypsin missed cleavages was allowed. Searches used a reversed sequence decoy strategy to control the peptide false discovery rate (FDR), with a 1% FDR threshold for identification. An unpaired t-test was used to calculate p-values for differential analysis, and volcano plots were generated based on log2 fold change and q-value (multiple testing corrected p-value). A q-value of ≤0.05 was considered the statistically significant cut-off.

The mass spectrometry proteomics data have been deposited to the ProteomeXchange Consortium via the PRIDE partner repository with the dataset identifier PXD056338.

Image processing, Analysis, and Statistics

Florescence images presented in this study are representative of cells imaged in at least three independent experiments and were processed with ImageJ software. The dimensions of some of the magnification insets or panels were enlarged using the *Scale* function on ImageJ.

Statistical analysis was performed with GraphPad Prism 10 software. Groups were compared using a two-tail unpaired Student *t* test and results were deemed significant when a p value was smaller than 0.05.

ACKNOWLEDGMENTS

We thank Thomas Melia and Shawn Ferguson (Yale) for discussion and advice, James Liu (Janelia Res Labs) for advice on endogenous tagging, Dario Alessi (Dundee, UK) for the personal communication of unpublished data and Chase Amos, Hanieh Falahati, and Berak Ugur (De Camilli lab) for critical reading of the manuscript. We also thank the support provided by the FIB-SEM Collaboration Core at Yale School of Medicine.

FUNDING

National Institutes of Health grant DA018343 (PDC)
National Institutes of Health grant NS36251 (PDC)
Aligning Science Across Parkinson's ASAP-000580 (PDC)
National Institutes of Health P30 CA008748 (MM)

AUTHOR CONTRIBUTIONS

Conceptualization: MGH, PDC
Methodology: MGH, PDC, HRC, ZI, MM, YW, CSX, SP
Investigation: MGH, HRC, ZI, MM, YW, CSX, SP
Figures: MGH, YW, HRC
Supervision: PDC, MM
Writing—original draft: MGH, PDC
Writing—review & editing: MGH, PDC, HRC, MM, CSX, SP

Competing Interests

PDC is a member of the Scientific Advisory Board of Casma Therapeutics. No conflict exists with this role.

FIGURE LEGENDS

Figure 1: Endogenous and exogenous BLTP3A form accumulations that associate with lysosomes.

(A) AlphaFold prediction of full-length BLTP3A with ConSurf conservation scores (top left) for each a.a. or cross-section of surface rendering of BLTP3A channel (top right) highlighting hydrophobic residues (orange). Linear representation of BLTP3A: per residue ConSurf scores (top) and RBG organization (bottom). IDR, predicted intrinsically disordered region (light gray); CH, C-terminal helix (dark gray).
(B) Alignment of the a.a. of motifs important for the indicated protein interactions of BLTP3B with corresponding sequences of BLTP3A. ConSurf conservation scores for each a.a. is indicated by color (same color scheme as in Fig.1A)
(C) Western blot of lysates of wild-type mouse tissues for BLTP3A, BLTP3B, and vinculin as a loading control.
(D) Western blot of control and edited (BLTP3A^V5) cell clones for BLTP3A, V5, and alpha-tubulin as a loading control.
(E) Fluorescence images of endogenously edited (left) or parental control (middle) A549 cells with antibodies against LAMP1 (green) and V5 (magenta). Scale bar, 10 μm. The insets are a zoom of a small region of the cell. Scale bar, 1 μm. Right: Fluorescence of exogenous BLTP3A-GFP (green) in endogenously edited A549 cell. Scale bar, 5 μm. Insets: zoom of square region of cell

894 showing co-localization of endogenous BLTP3A^V5 signal from immunolabeling with antibodies
895 against V5 (magenta) and BLTP3A-GFP fluorescence (green). Scale bar, 1 µm.
896 **(F)** Fluorescence image of wild-type RPE-1 cell immunostained with antibodies against LAMP1
897 (green) and DAPI (blue). Scale bar, 5 µm.
898 **(G)** Fluorescence image of an RPE-1 cell expressing exogenous BLTP3A-mRFP (large field,
899 inverted grays) and LAMP1-GFP (not shown). Scale bar, 5 µm. The area enclosed by a dotted
900 rectangle is shown at right at high magnification with BLTP3A-mRFP in magenta and LAMP1-
901 GFP in green (individual channels are shown as inverted grays). Red arrows indicate large
902 BLTP3A accumulations not associated with lysosomes. Scale bar, 1 µm.
903 **(H)** CLEM of a BLTP3A-mRFP positive cluster in an RPE-1 cell. Left: florescence images of
904 BLTP3A-mRFP (magenta). Scale bar, 1 µm. Right: EM micrograph of the field shown at left
905 revealing that the BLTP3A-mRFP fluorescence reflects clusters of small vesicles, many of them
906 tethered to the surface of lysosomes. Scale bar, 500 nm.
907 **(I)** Distance between the membranes of lysosomes and tethered vesicles from EM micrographs.
908 Mean = 10.8 nm; standard error of the mean = ±0.20 nm.
909 **(J)** Left: Fluorescence image of an RPE-1 cell expressing exogenous BLTP3A-mRFP (inverted
910 grays) and immunolabeled with antibodies against VAMP7 (shown in the high mag fields at right).
911 Scale bar, 5 µm. Right: zooms of different RPE-1 cells expressing exogenous BLTP3A-mRFP
912 (magenta) and immunolabeled (green) with antibodies against the following endogenous proteins,
913 VAMP4 and ATG9A. Individual channels are shown as inverted grays. Merge of channels on
914 bottom. Scale bar, 1 µm.
915
916 **Figure 2: The N-terminus of BLTP3A associates with Rab7 on the surface of lysosomes.**
917
918 **(A)** Fluorescence images of RPE-1 cells expressing exogenous BLTP3A-mRFP (shown in
919 inverted grays) and (not shown) GFP-tagged wild type Rab7 (left) or dominant negative (DN)
920 Rab7 (T22N) (right). Scale bar, 5 µm.
921 **(B)** CLEM of a BLTP3A-mRFP positive cluster in an RPE-1 cell expressing GFP-tagged dominant
922 negative Rab7. Left: fluorescence image (magenta). Scale bar, 1 µm. Right: EM micrograph of
923 the field shown at left revealing that the BLTP3A-mRFP fluorescence reflects clusters of small
924 vesicles. Scale bar, 500 nm.
925 **(C)** BLTP3 chimeras design. Left: Surface representation of the predicted RBG core of BLTP3A.
926 Red and blue indicate positive and negative charges, respectively, and gray indicates
927 hydrophobic surfaces. Right: Surface representation (top) and ribbon representation (bottom) of
928 the "untwisted" protein showing individual RBG motifs. Bottom: Cartoon of chimeras consisting of
929 BLTP3A (dark orange) and BLTP3B (light orange) RBG motifs.
930 **(D)** High-magnification live fluorescence images of RPE-1 cells expressing the indicated BLTP3-
931 mRFP constructs (magenta) and LAMP1-GFP (green). Individual channels are shown as inverted
932 grays. Scale bar, 1 µm.
933 **(E)** Ribbon representation of the AlphaFold prediction of a.a. 1-336 of BLTP3A. Blue indicates
934 loops connecting adjoining RBG motifs, and gray indicates the first beta-stand of the third RBG
935 motif.
936 **(F)** Fluorescence images (inverted grays) of RPE-1 cells expressing BLTP3A-1-336-mRFP and
937 either (not shown) GFP-Rab7 (left), or GFP-Rab7 T22N (right). Scale bar, 5 µm. A zoom of an

938 area of the cell at left (dotted square) expressing BLTP3A-1-336-mRFP (magenta) is also shown,
939 along with the Rab7 fluorescence (green), demonstrating the localization of BLTP3A-1-336-
940 mRFP around the entire profile of lysosomes. Individual channels are shown as inverted grays.
941 Scale bar, 2 μm.
942 **(G)** Cartoon depicting the proposed association of BLTP3A vesicle clusters with the surface of
943 lysosomes and the dependence of this association on Rab7.
944
945 **Figure 3: The C terminus of BLTP3A associates with vesicles**
946
947 **(A)** Top: Linear representation of BLTP3A RBG organization and C-terminal truncations indicated
948 by arrows. Bottom left: AlphaFold-based structure of the C terminus of BLTP3A channel.
949 Individual residues are colored by conservation scores as Fig. 1A. Truncations are indicated by
950 arrows. Bottom right: Fluorescence images (inverted grays) of RPE-1 cells expressing the
951 indicated BLTP3A-mRFP constructs along with dominant negative Rab7 (not shown)
952 demonstrating that the property of BLTP3A to bind and cluster vesicles is dependent on its region
953 comprised between a.a. 1327 and 1364. Note that the construct 1-1327, shows a focal
954 accumulation next to the nucleus, which is VAMP7 negative, likely reflecting its pool bound to
955 Rab45 (see Supplemental Figure 1A). Scale bar, 5 μm. Zoomed images (dotted squares) are
956 shown below the main field along with VAMP7 fluorescence. Scale bar, 1 μm.
957 **(B)** Western blots of cell extracts (inputs) of control and edited A549 cells, and of material
958 immunoisolated from these extracts by anti-V5 magnetic beads. Immunolabeling for BLTP3A, V5
959 (endogenously tagged BLTP3A), and for GAPDH as a loading control, are shown.
960 **(C)** Scatter plot of mass spectrometry-identified proteins in immunoisolated material from either
961 control or endogenously edited BLTP3A^V5 A549 cells using anti-V5 magnetic beads. Proteins
962 significantly enriched in material immunoisolated form edited cells compared to wild type cells are
963 plotted in the right-top quadrant. Proteins of note are labeled in magenta.
964
965 **Figure 4: Exogenous BLTP3A is shed from the surface of lysosomes upon damage of their**
966 **membranes.**
967
968 **(A)** Time-series of live fluorescence images (inverted grays) of exogenous BLTP3A-GFP and
969 mApple-IST1 before and after addition of LLOMe. Arrowheads (magenta) point to BLTP3A
970 accumulations shed from lysosomes upon addition of LLOMe. Scale bar, 5 μm.
971 **(B)** Time-series of live fluorescence images of BLTP3A-1-336-mRFP (magenta) and the
972 lysosomal marker NPC1-GFP (green). Fluorescence of individual channels is shown in inverted
973 grays. Scale bar, 2 μm.
974
975 **Figure 5: Activation of CASM recruits BLTP3A to the surface of damaged lysosomes**
976 **through an interaction with mATG8 proteins.**
977
978 **(A)** Alignment of the region of BLTP3A orthologues from different species centered on the a.a.
979 region required for mATG8 binding in human BLTP3A. The alignment shows a high degree of
980 conservation of the key residues of the LC3-interacting (LIR) motif among several chordates and
981 also observed in flies.

982 **(B)** Live fluorescence images (inverted grays) of RPE-1 cells expressing BLTP3A-mRFP (top) or
983 GFP-LC3B (bottom) in either fed (left) or starved (right) conditions. Arrows (magenta) indicate
984 GFP-LC3B positive foci. Scale bar, 5 µm.
985 **(C)** Time-series of live fluorescence images (inverted grays) of exogenous BLTP3A-mRFP and
986 GFP-LC3B before and after addition of LLOMe. Arrowheads point to lysosomes where BLTP3A
987 and LC3B decorate the entire lysosome profile upon addition of LLOMe. Scale bar, 5 µm.
988 **(D)** Time-series of live fluorescence images (inverted grays) of exogenous BLTP3AΔLIR-mRFP
989 and GFP-LC3B before and after addition of LLOMe. Arrowheads point to lysosomes where LC3B,
990 but not BLTP3A lacking a LIR motif, decorates the entire lysosome profile upon addition of
991 LLOMe. Scale bar, 5 µm.
992 **(E)** Correlative fluorescence-FIB-SEM microscopy of GFP-LC3B and BLTP3A-mRFP-positive
993 lysosomes in an RPE-1 cell 15 min after LLOMe addition. Left: Florescence image of an RPE-1
994 cell expressing GFP-LC3B (green), BLTP3A-mRFP (magenta), and mito-BFP (not shown), 15
995 min after addition of LLOMe. Scale bar, 5 µm. Region of cell for FIB-SEM marked by dotted line.
996 Middle: High magnification of the RPE-1 cell at left (blue square) showing both the BLTP3A-mRFP
997 (magenta) and the GFP-LC3B (green) channels. Individual channels are shown as inverted grays.
998 Merged channel also shows mito-BFP (blue) used for aligning EM and fluorescence images.
999 Scale bar, 2 µm. Right: EM reconstruction (scale bar, 1 µm) corresponding to the blue square
1000 from left. Lysosome, dark green; ER, yellow; mitochondria, blue; small vesicles, magenta.
1001 **(F)** Hypothetical model illustrating the different organization and orientation of BLTP3A on the
1002 surface of lysosomes depending on the state of the cell.
1003
1004 **Figure 6: Lysosomes are more susceptible to damage in cells lacking BLTP3A**
1005
1006 **(A)** Western blots of cell extracts (inputs) of control and edited A549 cells (BLTP3A KO clones)
1007 for the proteins indicated.
1008 **(B)** Fluorescence images of parental control (left) or BLTP3A KO (right) A549 cells with antibodies
1009 against LAMP1 (green). Scale bar, 20 µm. Is position of the lysosomes the same? They seem
1010 less disperse. Perhaps you could show a longer exposure of the KO? Is the effect the same in
1011 both clones?
1012 **(C)** Fluorescence images of parental control (top row) or BLTP3A KO (bottom row) A549 cells
1013 with antibodies against galectin-3 (inverted greys). Cells were treated with vehicle control (left
1014 column) or 1mM LLOMe (right column).
1015 **(D)** Quantification of galectin-3 spots per cell from field **C**. Error bars report the standard error of
1016 the mean (SEM). **, $p < 0.01$. Mean number of galectin-3 spots per cell and number of cells
1017 counted per condition indicated.
1018
1019
1020
1021 **SUPPLEMENTAL FIGURE LEGENDS**
1022
1023 **Supplemental Figure 1**
1024

1025 **(A)** Live fluorescence images (inverted grays) of RPE-1 cells expressing either GFP-Rab45 (left),
1026 BLTP3A-mRFP (center), or both proteins together (only BLTP3A is shown) (right) as indicated.
1027 Scale bar, 5 µm. High-magnification scale bar, 2 µm.
1028 **(B)** Genomic sequence of the edited BLTP3A locus (insertion of the V5 epitope) in A549 cell.
1029 Blue, small Gly-Ser linkers; green, V5 epitope sequence.
1030 **(C)** AlphaFold prediction of BLTP3A. The site where the V5 epitope (V904) was inserted is
1031 indicated. The long disordered sequence and the C-terminal helix are shown in gray.
1032 **(D)** Left: Fluorescence image of an RPE-1 cell expressing exogenous BLTP3B-mRFP (inverted
1033 grays) and immunolabeled with antibodies against endogenous VAMP7 (shown at right in the
1034 high magnification of the squared region in the main field). Scale bar, 5 µm. Right: zooms of
1035 different RPE-1 cells expressing exogenous BLTP3B-mRFP (magenta) and immunolabeled with
1036 antibodies (green) against endogenous VAMP4 or ATG9A. Individual channels are shown as
1037 inverted grays. Merge of channels on bottom. Scale bar, 1 µm.
1038 **(E)** Live fluorescence image of RPE-1 cell expressing exogenous RFP-LRRK1^{K746G} (green), which
1039 is primarily cytosolic. Scale bar, 5 µm.
1040 **(F)** Live fluorescence images (inverted grays) of RPE-1 cells expressing exogenous GFP-
1041 LRRK1^{K746G} (left) and BLTP3A-mRFP (right). Scale bar, 10 µm. High magnifications of areas of
1042 overlap (orange box) or no overlap (blue box) of the fluorescence of exogenous LRRK1 (green)
1043 and BLTP3A (magenta) are shown at right. Scale bar, 2 µm.
1044 **(G)** RPE-1 cell expressing BLTP3A-mRFP, GFP-LRRK1^{K746G} and mito-BFP. CLEM of a BLTP3A-
1045 mRFP and GFP-LRRK1^{K746G} positive region showing abundance of small vesicles associated with
1046 lysosomes in the corresponding EM image. The mito-BFP fluorescence is not shown and was
1047 used for alignment. Scale bar, 2 µm for the fluorescence and 500 nm for the EM).
1048 **(H)** Western blot of lysate of RPE-1 cells expressing exogenous RFP-LRRK1^{K746G} or RFP-
1049 LRRK1^{D1409A} for RFP (to detect LRRK1 fusions), Rab7, phospho-Rab7 S72, and alpha-tubulin as
1050 a loading control.
1051
1052 **Supplemental Figure 2**
1053
1054 **(A)** Live fluorescence image (inverted grays) of RPE-1 cells expressing GFP-LRRK2 (left) and
1055 BLTP3A-mRFP (right). Scale bar, 10 µm. High magnifications of areas of overlap (orange box) or
1056 no overlap (blue box) of the LRRK2 (green) and BLTP3A (magenta) fluorescence. Scale bar, 2
1057 µm.
1058 **(B)** Live fluorescence image (inverted grays) of COS7 cells expressing GFP-LRRK2 (left) and
1059 BLTP3A-mRFP (right). Scale bar, 5 µm. High magnifications of areas of overlap (orange box) or
1060 no overlap (blue box) of the LRRK2 (green) and BLTP3A (magenta) fluorescence. Scale bar, 2
1061 µm.
1062 **(C)** Fluorescence images of RPE-1 cells expressing the indicated BLTP3A-mRFP construct.
1063 Scale bar, 5 µm
1064 **(D)** AlphaFold3 multimer prediction of full-length MAP1LC3B (green) and a.a. 1110-1150 of
1065 BLTP3A (magenta). Arrows indicate key residues of the LIR motif of BLTP3A.
1066 **(E)** AlphaFold3 multimer predictions of mATG8 proteins and a.a. 1110-1150 of BLTP3A with and
1067 without the LIR motif (ΔLIR).
1068

1069 **Supplemental Figure 3**
1070
1071 **(A)** Time-series of live fluorescence images (inverted grays) of BLTP3A-mRFP and GFP-LC3B
1072 before and after addition of GPN. Arrowheads point to lysosomes where BLTP3A and LC3B
1073 decorate the entire profile upon addition of GPN. Time, seconds. Scale bar, 5 μm.
1074 **(B)** CLEM of GFP-LC3B and BLTP3A-mRFP-positive lysosomes in an RPE-1 cell 15 min after
1075 LLOMe addition. Left: Florescence image of an RPE-1 cell expressing BLTP3A-mRFP (magenta),
1076 GFP-LC3B (green), and mito-BFP (not shown), 15 min after addition of LLOMe. Scale bar, 2 μm.
1077 Middle: High magnification of the RPE-1 cell at left (blue square) showing both the BLTP3A-mRFP
1078 (magenta) and the GFP-LC3B (green) channels. Individual channels are shown as inverted grays.
1079 Scale bar, 1 μm. Right: EM image (scale bar, 200 nm) corresponding to the high magnification
1080 fluorescence images. Note presence of some small vesicles (magenta arrows) in spite of BLTP3A
1081 fluorescence around the lysosomes.
1082 **(C)** Genomic sequence of the edited BLTP3A locus in A549 cell. Blue, gRNA; green, PAM; red,
1083 indel mutations.
1084 **(D)** Quantification of relative LAMP1 expression from western blots (n=3) of Figure 6A. Error bars
1085 indicate the standard error of the mean (SEM).
1086
1087 **Supplemental Movie 1**
1088 FIB-SEM reconstruction of GFP-LC3B and BLTP3A-mRFP-positive lysosomes in an RPE-1 cell
1089 15 min after LLOMe addition (from Figure 5E). Reconstructed organelle colors: lysosome, dark
1090 green; ER, yellow; mitochondria, blue; small vesicles, magenta; large vesicles, green. Scale bar,
1091 1 μm.
1092
1093 **Supplemental Movie 2**
1094 FIB-SEM image stack of the region used for the reconstruction in Figure 5E and Supplemental
1095 Movie 1. Lysosomes are pseudo-colored dark green. Scale bar, 1 μm.

REFERENCES

Abramson, J., J. Adler, J. Dunger, R. Evans, T. Green, A. Pritzel, O. Ronneberger, L. Willmore, A.J. Ballard, J. Bambrick, S.W. Bodenstein, D.A. Evans, C.-C. Hung, M. O'Neill, D. Reiman, K. Tunyasuvunakool, Z. Wu, A. Žemgulytė, E. Arvaniti, C. Beattie, O. Bertolli, A. Bridgland, A. Cherepanov, M. Congreve, A.I. Cowen-Rivers, A. Cowie, M. Figurnov, F.B. Fuchs, H. Gladman, R. Jain, Y.A. Khan, C.M.R. Low, K. Perlin, A. Potapenko, P. Savy, S. Singh, A. Stecula, A. Thillaisundaram, C. Tong, S. Yakneen, E.D. Zhong, M. Zielinski, A. Žídek, V. Bapst, P. Kohli, M. Jaderberg, D. Hassabis, and J.M. Jumper. 2024. Accurate structure prediction of biomolecular interactions with AlphaFold 3. *Nature*. 630:493–500. doi:10.1038/s41586-024-07487-w.

Adlakha, J., Z. Hong, P. Li, and K.M. Reinisch. 2022. Structural and biochemical insights into lipid transport by VPS13 proteins. *Journal of Cell Biology*. 221:e202202030. doi:10.1083/jcb.202202030.

Advani, R.J., B. Yang, R. Prekeris, K.C. Lee, J. Klumperman, and R.H. Scheller. 1999. Vamp-7 Mediates Vesicular Transport from Endosomes to Lysosomes. *Journal of Cell Biology*. 146:765–776. doi:10.1083/jcb.146.4.765.

Anding, A.L., C. Wang, T.-K. Chang, D.A. Sliter, C.M. Powers, K. Hofmann, R.J. Youle, and E.H. Baehrecke. 2018. Vps13D Encodes a Ubiquitin-Binding Protein that Is Required for the Regulation of Mitochondrial Size and Clearance. *Current Biology*. 28:287-295.e6. doi:10.1016/j.cub.2017.11.064.

Armon, A., D. Graur, and N. Ben-Tal. 2001. ConSurf: an algorithmic tool for the identification of functional regions in proteins by surface mapping of phylogenetic information1. *Journal of Molecular Biology*. 307:447–463. doi:10.1006/jmbi.2000.4474.

Bahadoran, P., E. Aberdam, F. Mantoux, R. Buscà, K. Bille, N. Yalman, G. de Saint-Basile, R. Casaroli-Marano, J.-P. Ortonne, and R. Ballotti. 2001. Rab27a: A Key to Melanosome Transport in Human Melanocytes. *Journal of Cell Biology*. 152:843–850. doi:10.1083/jcb.152.4.843.

Baldwin, H.A., C. Wang, G. Kanfer, H.V. Shah, A. Velayos-Baeza, M. Dulovic-Mahlow, N. Brüggemann, A. Anding, E.H. Baehrecke, D. Maric, W.A. Prinz, and R.J. Youle. 2021. VPS13D promotes peroxisome biogenesis. *Journal of Cell Biology*. 220:e202001188. doi:10.1083/jcb.202001188.

Banerjee, S., S. Daetwyler, X. Bai, M. Michaud, J. Jouhet, S. Madhugiri, E. Johnson, C.-W. Wang, R. Fiolka, A. Toulmay, and W.A. Prinz. 2024. The Vps13-like protein BLTP2 is pro-survival and regulates phosphatidylethanolamine levels in the plasma membrane to maintain its fluidity and function. 2024.02.04.578804. doi:10.1101/2024.02.04.578804.

Bentley-DeSousa, A., and S.M. Ferguson. 2023. A STING-CASM-GABARAP Pathway Activates LRRK2 at Lysosomes. 2023.10.31.564602. doi:10.1101/2023.10.31.564602.

Boyle, K.B., C.J. Ellison, P.R. Elliott, M. Schuschnig, K. Grimes, M.S. Dionne, C. Sasakawa, S. Munro, S. Martens, and F. Randow. 2023. TECPR1 conjugates LC3 to damaged endomembranes upon detection of sphingomyelin exposure. *The EMBO Journal*. 42:e113012. doi:10.15252/embj.2022113012.

1138 Cai, S., Y. Wu, A. Guillen-Samander, W. Hancock-Cerutti, J. Liu, and P.D. Camilli. 2022a. In situ
1139 architecture of the lipid transport protein VPS13C at ER-lysosomes membrane contacts.
1140 2022.03.08.482579. doi:10.1101/2022.03.08.482579.

1141 Cai, S., Y. Wu, A. Guillén-Samander, W. Hancock-Cerutti, J. Liu, and P. De Camilli. 2022b. In situ
1142 architecture of the lipid transport protein VPS13C at ER–lysosome membrane contacts.
1143 *Proceedings of the National Academy of Sciences*. 119:e2203769119.
1144 doi:10.1073/pnas.2203769119.

1145 Carter, A.P., A.G. Diamant, and L. Urnavicius. 2016. How dynein and dynactin transport cargos:
1146 a structural perspective. *Current Opinion in Structural Biology*. 37:62–70.
1147 doi:10.1016/j.sbi.2015.12.003.

1148 Chen, W., M.M. Motsinger, J. Li, K.P. Bohannon, and P.I. Hanson. 2024. Ca2+-sensor ALG-2
1149 engages ESCRTs to enhance lysosomal membrane resilience to osmotic stress.
1150 *Proceedings of the National Academy of Sciences*. 121:e2318412121.
1151 doi:10.1073/pnas.2318412121.

1152 Corkery, D.P., S. Castro-Gonzalez, A. Knyazeva, L.K. Herzog, and Y. Wu. 2023. An ATG12-
1153 ATG5-TECPR1 E3-like complex regulates unconventional LC3 lipidation at damaged
1154 lysosomes. *EMBO reports*. 24:e56841. doi:10.15252/embr.202356841.

1155 Corkery, D.P., S. Li, D. Wijayatunga, L.K. Herzog, A. Knyazeva, and Y.-W. Wu. 2024. ESCRT
1156 recruitment to damaged lysosomes is dependent on the ATG8 E3-like ligases.
1157 2024.04.30.591897. doi:10.1101/2024.04.30.591897.

1158 Cross, J., J. Durgan, D.G. McEwan, M. Tayler, K.M. Ryan, and O. Florey. 2023. Lysosome
1159 damage triggers direct ATG8 conjugation and ATG2 engagement via non-canonical
1160 autophagy. *Journal of Cell Biology*. 222:e202303078. doi:10.1083/jcb.202303078.

1161 De Camilli, P., F. Benfenati, F. Valtorta, and P. Greengard. 1990. The Synapsins. *Annual Review*
1162 *of Cell and Developmental Biology*. 6:433–460.
1163 doi:10.1146/annurev.cb.06.110190.002245.

1164 DeGrella, R.F., and R.D. Simoni. 1982. Intracellular transport of cholesterol to the plasma
1165 membrane. *Journal of Biological Chemistry*. 257:14256–14262. doi:10.1016/S0021-
1166 9258(19)45374-X.

1167 Deretic, V., T. Duque, E. Trosdal, M. Paddar, R. Javed, and P. Akepati. 2024. Membrane
1168 atg8ylation in Canonical and Noncanonical Autophagy. *Journal of Molecular Biology*.
1169 436:168532. doi:10.1016/j.jmb.2024.168532.

1170 Durgan, J., and O. Florey. 2022. Many roads lead to CASM: Diverse stimuli of noncanonical
1171 autophagy share a unifying molecular mechanism. *Science Advances*. 8:eabo1274.
1172 doi:10.1126/sciadv.abo1274.

1173 Dziurdzik, S.K., and E. Conibear. 2021. The Vps13 Family of Lipid Transporters and Its Role at
1174 Membrane Contact Sites. *International Journal of Molecular Sciences*. 22:2905.
1175 doi:10.3390/ijms22062905.

1176 Figueras-Novoa, C., L. Timimi, E. Marcassa, R. Ulferts, and R. Beale. 2024. Conjugation of
1177 ATG8s to single membranes at a glance. *Journal of Cell Science*. 137:jcs261031.
1178 doi:10.1242/jcs.261031.

1179 Filippini, F., S. Nola, A. Zahraoui, K. Roger, M. Esmaili, J. Sun, J. Wojnacki, A. Vlieghe, P. Bun,
1180 S. Blanchon, J.-C. Rain, J.-M. Taymans, M.-C. Chartier-Harlin, C. Guerrera, and T. Galli.
1181 2023. Secretion of VGF relies on the interplay between LRRK2 and post-Golgi v-SNAREs.
1182 *Cell Reports*. 42:112221. doi:10.1016/j.celrep.2023.112221.

1183 Fischer, T.D., C. Wang, B.S. Padman, M. Lazarou, and R.J. Youle. 2020. STING induces LC3B
1184 lipidation onto single-membrane vesicles via the V-ATPase and ATG16L1-WD40 domain.
1185 *Journal of Cell Biology*. 219:e202009128. doi:10.1083/jcb.202009128.

1186 Fujita, K., S. Kedashiro, T. Yagi, N. Hisamoto, K. Matsumoto, and H. Hanafusa. 2022. The ULK
1187 complex–LRRK1 axis regulates Parkin-mediated mitophagy via Rab7 Ser-72
1188 phosphorylation. *Journal of Cell Science*. 135:jcs260395. doi:10.1242/jcs.260395.

1189 Gateva, V., J.K. Sandling, G. Hom, K.E. Taylor, S.A. Chung, X. Sun, W. Ortmann, R. Kosoy, R.C.
1190 Ferreira, G. Nordmark, I. Gunnarsson, E. Svenungsson, L. Padyukov, G. Sturfelt, A.
1191 Jönsen, A.A. Bengtsson, S. Rantapää-Dahlqvist, E.C. Baechler, E.E. Brown, G.S.
1192 Alarcón, J.C. Edberg, R. Ramsey-Goldman, G. McGwin, J.D. Reveille, L.M. Vilá, R.P.
1193 Kimberly, S. Manzi, M.A. Petri, A. Lee, P.K. Gregersen, M.F. Seldin, L. Rönnblom, L.A.
1194 Criswell, A.-C. Syvänen, T.W. Behrens, and R.R. Graham. 2009. A large-scale replication
1195 study identifies TNIP1, PRDM1, JAZF1, UHRF1BP1 and IL10 as risk loci for systemic
1196 lupus erythematosus. *Nat Genet*. 41:1228–1233. doi:10.1038/ng.468.

1197 Gillingham, A.K., J. Bertram, F. Begum, and S. Munro. 2019. In vivo identification of GTPase
1198 interactors by mitochondrial relocalization and proximity biotinylation. *eLife*. 8:e45916.
1199 doi:10.7554/eLife.45916.

1200 Goldman, R., and A. Kaplan. 1973. Rupture of rat liver lysosomes mediated by l-amino acid
1201 esters. *Biochimica et Biophysica Acta (BBA) - Biomembranes*. 318:205–216.
1202 doi:10.1016/0005-2736(73)90114-4.

1203 Gómez-Sánchez, R., J. Rose, R. Guimarães, M. Mari, D. Papinski, E. Rieter, W.J. Geerts, R.
1204 Hardenberg, C. Kraft, C. Ungermann, and F. Reggiori. 2018. Atg9 establishes Atg2-
1205 dependent contact sites between the endoplasmic reticulum and phagophores. *The*
1206 *Journal of cell biology*. jcb.201710116. doi:10.1083/jcb.201710116.

1207 Guillén-Samander, A., M. Leonzino, M.G. Hanna IV, N. Tang, H. Shen, and P. De Camilli. 2021.
1208 VPS13D bridges the ER to mitochondria and peroxisomes via Miro. *Journal of Cell*
1209 *Biology*. 220. doi:10.1083/jcb.202010004.

1210 Guillén-Samander, A., Y. Wu, S.S. Pineda, F.J. García, J.N. Eisen, M. Leonzino, B. Ugur, M.
1211 Kellis, M. Heiman, and P. De Camilli. 2022. A partnership between the lipid scramblase
1212 XK and the lipid transfer protein VPS13A at the plasma membrane. *Proceedings of the*
1213 *National Academy of Sciences*. 119:e2205425119. doi:10.1073/pnas.2205425119.

1214 Hanna, M., A. Guillén-Samander, and P. De Camilli. 2023. RBG Motif Bridge-Like Lipid Transport
1215 Proteins: Structure, Functions, and Open Questions. *Annu. Rev. Cell Dev. Biol.*
1216 doi:10.1146/annurev-cellbio-120420-014634.

1217 Hanna, M.G., P.H. Suen, Y. Wu, K.M. Reinisch, and P. De Camilli. 2022. SHIP164 is a chorein
1218 motif lipid transfer protein that controls endosome–Golgi membrane traffic. *Journal of Cell*
1219 *Biology*. 221:e202111018. doi:10.1083/jcb.202111018.

1220 Heo, J.-M., A. Ordureau, S. Swarup, J.A. Paulo, K. Shen, D.M. Sabatini, and J.W. Harper. 2018.
1221 RAB7A phosphorylation by TBK1 promotes mitophagy via the PINK-PARKIN pathway.
1222 *Science Advances*. 4:eaav0443. doi:10.1126/sciadv.aav0443.

1223 Herbst, S., P. Campbell, J. Harvey, E.M. Bernard, V. Papayannopoulos, N.W. Wood, H.R. Morris,
1224 and M.G. Gutierrez. 2020. LRRK2 activation controls the repair of damaged
1225 endomembranes in macrophages. *The EMBO Journal*. 39:e104494.
1226 doi:10.15252/embj.2020104494.

1227 Hume, A.N., L.M. Collinson, A. Rapak, A.Q. Gomes, C.R. Hopkins, and M.C. Seabra. 2001.
1228 Rab27a Regulates the Peripheral Distribution of Melanosomes in Melanocytes. *Journal of*
1229 *Cell Biology*. 152:795–808. doi:10.1083/jcb.152.4.795.

1230 John Peter, A.T., B. Herrmann, D. Antunes, D. Rapaport, K.S. Dimmer, and B. Kornmann. 2017.
1231 Vps13-Mcp1 interact at vacuole–mitochondria interfaces and bypass ER–mitochondria
1232 contact sites. *J Cell Biol*. 216:3219–3229. doi:10.1083/jcb.201610055.

1233 John Peter, A.T., S.N.S. van Schie, N.J. Cheung, A.H. Michel, M. Peter, and B. Kornmann. 2022.
1234 Rewiring phospholipid biosynthesis reveals resilience to membrane perturbations and
1235 uncovers regulators of lipid homeostasis. *The EMBO Journal*. 41:e109998.
1236 doi:10.15252/embj.2021109998.

1237 Johnston, P.A., R. Jahn, and T.C. Südhof. 1989. Transmembrane Topography and Evolutionary
1238 Conservation of Synaptophysin. *Journal of Biological Chemistry*. 264:1268–1273.
1239 doi:10.1016/S0021-9258(19)85081-0.

1240 Jumper, J., R. Evans, A. Pritzel, T. Green, M. Figurnov, O. Ronneberger, K. Tunyasuvunakool,
1241 R. Bates, A. Žídek, A. Potapenko, A. Bridgland, C. Meyer, S.A.A. Kohl, A.J. Ballard, A.
1242 Cowie, B. Romera-Paredes, S. Nikolov, R. Jain, J. Adler, T. Back, S. Petersen, D. Reiman,
1243 E. Clancy, M. Zielinski, M. Steinegger, M. Pacholska, T. Berghammer, S. Bodenstein, D.
1244 Silver, O. Vinyals, A.W. Senior, K. Kavukcuoglu, P. Kohli, and D. Hassabis. 2021. Highly
1245 accurate protein structure prediction with AlphaFold. *Nature*. 596:583–589.
1246 doi:10.1038/s41586-021-03819-2.

1247 Kang, Y., K.S. Lehmann, J. Vanegas, H. Long, A. Jefferson, M.A. Freeman, and S. Clark. 2024.
1248 Structural basis of bulk lipid transfer by bridge-like lipid transfer protein LPD-3.
1249 2024.06.21.600134. doi:10.1101/2024.06.21.600134.

1250 Kaur, N., L.R. de la Ballina, H.S. Haukaas, M.L. Torgersen, M. Radulovic, M.J. Munson, A.
1251 Sabirsh, H. Stenmark, A. Simonsen, S.R. Carlsson, and A.H. Lystad. 2023. TECPR1 is
1252 activated by damage-induced sphingomyelin exposure to mediate
1253 noncanonical autophagy. *The EMBO Journal*. 42:e113105.
1254 doi:10.15252/embj.2022113105.

1255 Kumar, N., M. Leonzino, W. Hancock-Cerutti, F.A. Horenkamp, P. Li, J.A. Lees, H. Wheeler, K.M.
1256 Reinisch, and P.D. Camilli. 2018. VPS13A and VPS13C are lipid transport proteins

differentially localized at ER contact sites. *The Journal of cell biology*. 217:3625–3639. doi:10.1083/jcb.201807019.

Leonzino, M., K.M. Reinisch, and P. De Camilli. 2021. Insights into VPS13 properties and function reveal a new mechanism of eukaryotic lipid transport. *Biochimica et Biophysica Acta (BBA) - Molecular and Cell Biology of Lipids*. 1866:159003. doi:10.1016/j.bbalip.2021.159003.

Levine, T.P. 2019. Remote homology searches identify bacterial homologues of eukaryotic lipid transfer proteins, including Chorein-N domains in TamB and AsmA and Mdm31p. *BMC Molecular and Cell Biology*. 20. doi:10.1186/s12860-019-0226-z.

Levine, T.P. 2022. Sequence Analysis and Structural Predictions of Lipid Transfer Bridges in the Repeating Beta Groove (RBG) Superfamily Reveal Past and Present Domain Variations Affecting Form, Function and Interactions of VPS13, ATG2, SHIP164, Hobbit and Tweek. *Contact*. 5:25152564221134328. doi:10.1177/25152564221134328.

Li, P., J.A. Lees, C.P. Lusk, and K.M. Reinisch. 2020. Cryo-EM reconstruction of a VPS13 fragment reveals a long groove to channel lipids between membranes. *Journal of Cell Biology*. 219. doi:10.1083/jcb.202001161.

Lin, S.X., W.G. Mallet, A.Y. Huang, and F.R. Maxfield. 2003. Endocytosed Cation-Independent Mannose 6-Phosphate Receptor Traffics via the Endocytic Recycling Compartment en Route to the trans-Golgi Network and a Subpopulation of Late Endosomes. *MBoC*. 15:721–733. doi:10.1091/mbc.e03-07-0497.

Maeda, S., C. Otomo, and T. Otomo. 2019. The autophagic membrane tether ATG2A transfers lipids between membranes. *eLife*. 8:e45777. doi:10.7554/eLife.45777.

Mallard, F., B.L. Tang, T. Galli, D. Tenza, A. Saint-Pol, X. Yue, C. Antony, W. Hong, B. Goud, and L. Johannes. 2002. Early/recycling endosomes-to-TGN transport involves two SNARE complexes and a Rab6 isoform. *The Journal of cell biology*. 156:653–664. doi:10.1083/jcb.200110081.

Martinez-Arca, S., S. Coco, G. Mainguy, U. Schenk, P. Alberts, P. Bouillé, M. Mezzina, A. Prochiantz, M. Matteoli, D. Louvard, and T. Galli. 2001. A Common Exocytotic Mechanism Mediates Axonal and Dendritic Outgrowth. *J. Neurosci.* 21:3830–3838. doi:10.1523/JNEUROSCI.21-11-03830.2001.

Melia, T.J., A.H. Lystad, and A. Simonsen. 2020. Autophagosome biogenesis: From membrane growth to closure. *Journal of Cell Biology*. 219:e202002085. doi:10.1083/jcb.202002085.

Ménasché, G., E. Pastural, J. Feldmann, S. Certain, F. Ersoy, S. Dupuis, N. Wulffraat, D. Bianchi, A. Fischer, F. Le Deist, and G. de Saint Basile. 2000. Mutations in RAB27A cause Griscelli syndrome associated with haemophagocytic syndrome. *Nat Genet*. 25:173–176. doi:10.1038/76024.

Meyer, H., and B. Kravic. 2024. The Endo-Lysosomal Damage Response. *Annual Review of Biochemistry*. 93:367–387. doi:10.1146/annurev-biochem-030222-102505.

1295 Milovanovic, D., and P. De Camilli. 2017. Synaptic Vesicle Clusters at Synapses: A Distinct Liquid
1296 Phase? *Neuron*. 93:995–1002. doi:10.1016/j.neuron.2017.02.013.

1297 Milovanovic, D., Y. Wu, X. Bian, and P. De Camilli. 2018. A liquid phase of synapsin and lipid
1298 vesicles. *Science*. 361:604–607. doi:10.1126/science.aat5671.

1299 Nagashima, K., S. Torii, Z. Yi, M. Igarashi, K. Okamoto, T. Takeuchi, and T. Izumi. 2002.
1300 Melanophilin directly links Rab27a and myosin Va through its distinct coiled-coil regions.
1301 *FEBS Letters*. 517:233–238. doi:10.1016/S0014-5793(02)02634-0.

1302 Nagata, K., T. Satoh, H. Itoh, T. Kozasa, Y. Okano, T. Doi, Y. Kaziro, and Y. Nozawa. 1990. The
1303 ram: A novel low molecular weight GTP-binding protein cDNA from a rat megakaryocyte
1304 library. *FEBS Letters*. 275:29–32. doi:10.1016/0014-5793(90)81431-M.

1305 Neuman, S.D., T.P. Levine, and A. Bashirullah. 2022. A novel superfamily of bridge-like lipid
1306 transfer proteins. *Trends in Cell Biology*. 32:962–974. doi:10.1016/j.tcb.2022.03.011.

1307 Nieto-Torres, J.L., A.M. Leidal, J. Debnath, and M. Hansen. 2021. Beyond Autophagy: The
1308 Expanding Roles of ATG8 Proteins. *Trends in Biochemical Sciences*. 46:673–686.
1309 doi:10.1016/j.tibs.2021.01.004.

1310 Nirujogi, R.S., F. Tonelli, M. Taylor, P. Lis, A. Zimprich, E. Sammler, and D.R. Alessi. 2021.
1311 Development of a multiplexed targeted mass spectrometry assay for LRRK2-
1312 phosphorylated Rabs and Ser910/Ser935 biomarker sites. *Biochemical Journal*. 478:299–
1313 326. doi:10.1042/BCJ20200930.

1314 Osawa, T., T. Kotani, T. Kawaoka, E. Hirata, K. Suzuki, H. Nakatogawa, Y. Ohsumi, and N.N.
1315 Noda. 2019. Atg2 mediates direct lipid transfer between membranes for autophagosome
1316 formation. *Nat Struct Mol Biol*. 26:281–288. doi:10.1038/s41594-019-0203-4.

1317 Otto, G.P., M. Razi, J. Morvan, F. Stenner, and S.A. Tooze. 2010. A novel syntaxin 6-interacting
1318 protein, SHIP164, regulates syntaxin 6-dependent sorting from early endosomes. *Traffic*
1319 *(Copenhagen, Denmark)*. 11:688–705. doi:10.1111/j.1600-0854.2010.01049.x.

1320 Palade, G. 1975. Intracellular Aspects of the Process of Protein Synthesis. *Science*. 189:347–
1321 358. doi:10.1126/science.1096303.

1322 Pang, S., and C.S. Xu. 2023. Chapter 11 - Methods of enhanced FIB-SEM sample preparation
1323 and image acquisition. K. Narayan, L. Collinson, and P. Verkade, editors. Academic Press.

1324 Park, D., Y. Wu, S.-E. Lee, G. Kim, S. Jeong, D. Milovanovic, P. De Camilli, and S. Chang. 2021.
1325 Cooperative function of synaptophysin and synapsin in the generation of synaptic vesicle-
1326 like clusters in non-neuronal cells. *Nat Commun*. 12:263. doi:10.1038/s41467-020-20462-
1327 z.

1328 Park, J.-S., and A.M. Neiman. 2012. VPS13 regulates membrane morphogenesis during
1329 sporulation in Saccharomyces cerevisiae. *Journal of Cell Science*. 125:3004–3011.
1330 doi:10.1242/jcs.105114.

1331 Park, J.-S., M.K. Thorsness, R. Policastro, L.L. McGoldrick, N.M. Hollingsworth, P.E. Thorsness,
1332 and A.M. Neiman. 2016. Yeast Vps13 promotes mitochondrial function and is localized at
1333 membrane contact sites. *MBoC*. 27:2435–2449. doi:10.1091/mbc.E16-02-0112.

1334 Pols, M.S., E. van Meel, V. Oorschot, C. ten Brink, M. Fukuda, M.G. Swetha, S. Mayor, and J.
1335 Klumperman. 2013. hVps41 and VAMP7 function in direct TGN to late endosome
1336 transport of lysosomal membrane proteins. *Nat Commun*. 4:1361.
1337 doi:10.1038/ncomms2360.

1338 Prinz, W.A., A. Toulmay, and T. Balla. 2020. The functional universe of membrane contact sites.
1339 *Nature Reviews Molecular Cell Biology*. 21:7–24. doi:10.1038/s41580-019-0180-9.

1340 Radulovic, M., K.O. Schink, E.M. Wenzel, V. Nähse, A. Bongiovanni, F. Lafont, and H. Stenmark.
1341 2018. ESCRT-mediated lysosome repair precedes lysophagy and promotes cell survival.
1342 *The EMBO Journal*. 37:e99753. doi:10.15252/embj.201899753.

1343 Radulovic, M., E.M. Wenzel, S. Gilani, L.K. Holland, A.H. Lystad, S. Phuyal, V.M. Olkkonen, A.
1344 Brech, M. Jäättelä, K. Maeda, C. Raiborg, and H. Stenmark. 2022. Cholesterol transfer
1345 via endoplasmic reticulum contacts mediates lysosome damage repair. *The EMBO*
1346 *Journal*. 41:e112677. doi:10.15252/embj.2022112677.

1347 Reinisch, K., P. De Camilli, and T. Melia. 2024. Lipid dynamics at membrane contact sites. *Annu.*
1348 *Rev. Biochem.*

1349 Saheki, Y., and P.D. Camilli. 2017. Endoplasmic Reticulum-Plasma Membrane Contact Sites.
1350 *Annual review of biochemistry*. 86:659–684. doi:10.1146/annurev-biochem-061516-
1351 044932.

1352 Shukla, S., K.P. Larsen, C. Ou, K. Rose, and J.H. Hurley. 2022. In vitro reconstitution of calcium-
1353 dependent recruitment of the human ESCRT machinery in lysosomal membrane repair.
1354 *Proceedings of the National Academy of Sciences*. 119:e2205590119.
1355 doi:10.1073/pnas.2205590119.

1356 Skowyra, M.L., P.H. Schlesinger, T.V. Naismith, and P.I. Hanson. 2018. Triggered recruitment of
1357 ESCRT machinery promotes endolysosomal repair. *Science*. 360:eaar5078.
1358 doi:10.1126/science.aar5078.

1359 Stenmark, H., and V.M. Olkkonen. 2001. The Rab GTPase family. *Genome Biology*.
1360 2:reviews3007.1. doi:10.1186/gb-2001-2-5-reviews3007.

1361 Strom, M., A.N. Hume, A.K. Tarafder, E. Barkagianni, and M.C. Seabra. 2002. A Family of Rab27-
1362 binding Proteins: MELANOPHILIN LINKS Rab27a AND MYOSIN Va FUNCTION IN
1363 MELANOSOME TRANSPORT*. *Journal of Biological Chemistry*. 277:25423–25430.
1364 doi:10.1074/jbc.M202574200.

1365 Südhof, T.C., A.J. Czernik, H.-T. Kao, K. Takei, P.A. Johnston, A. Horiuchi, S.D. Kanazir, M.A.
1366 Wagner, M.S. Perin, P. De Camilli, and P. Greengard. 1989. Synapsins: Mosaics of
1367 Shared and Individual Domains in a Family of Synaptic Vesicle Phosphoproteins. *Science*.
1368 245:1474–1480. doi:10.1126/science.2506642.

1369 Talaia, G., A. Bentley-DeSousa, and S.M. Ferguson. 2024. Lysosomal TBK1 responds to amino
1370 acid availability to relieve Rab7-dependent mTORC1 inhibition. *The EMBO Journal*. 1–20.
1371 doi:10.1038/s44318-024-00180-8.

1372 Tan, J.X., and T. Finkel. 2022. A phosphoinositide signalling pathway mediates rapid lysosomal
1373 repair. *Nature*. 1–7. doi:10.1038/s41586-022-05164-4.

1374 Thiele, D.L., and P.E. Lipsky. 1990. Mechanism of L-leucyl-L-leucine methyl ester-mediated killing
1375 of cytotoxic lymphocytes: dependence on a lysosomal thiol protease, dipeptidyl peptidase
1376 I, that is enriched in these cells. *Proceedings of the National Academy of Sciences*. 87:83–
1377 87. doi:10.1073/pnas.87.1.83.

1378 Tokai, M., H. Kawasaki, Y. Kikuchi, and K. Ouchi. 2000. Cloning and Characterization of the CSF1
1379 Gene ofSaccharomyces cerevisiae, Which Is Required for Nutrient Uptake at Low
1380 Temperature. *Journal of Bacteriology*. 182:2865–2868. doi:10.1128/JB.182.10.2865-
1381 2868.2000.

1382 Tran, T.H.T., Q. Zeng, and W. Hong. 2007. VAMP4 cycles from the cell surface to the trans-Golgi
1383 network via sorting and recycling endosomes. *Journal of Cell Science*. 120:1028–1041.
1384 doi:10.1242/jcs.03387.

1385 Tu, Y.X., and J. Brumell. 2020. Examining the Autophagy Proximity Interactome. University of
1386 Toronto.

1387 Uchimoto, T., H. Nohara, R. Kamehara, M. Iwamura, N. Watanabe, and Y. Kobayashi. 1999.
1388 Mechanism of apoptosis induced by a lysosomotropic agent, L-Leucyl-L-Leucine methyl
1389 ester. *Apoptosis*. 4:357–362. doi:https://doi.org/10.1023/A:1009695221038.

1390 Unoki, M., T. Nishidate, and Y. Nakamura. 2004. ICBP90, an E2F-1 target, recruits HDAC1 and
1391 binds to methyl-CpG through its SRA domain. *Oncogene*. 23:7601–7610.
1392 doi:10.1038/sj.onc.1208053.

1393 Valverde, D.P., S. Yu, V. Boggavarapu, N. Kumar, J.A. Lees, T. Walz, K.M. Reinisch, and T.J.
1394 Melia. 2019. ATG2 transports lipids to promote autophagosome biogenesis.
1395 *Journal of Cell Biology*. 218:1787–1798. doi:10.1083/jcb.201811139.

1396 Velikkakath, A.K.G., T. Nishimura, E. Oita, N. Ishihara, and N. Mizushima. 2012. Mammalian Atg2
1397 proteins are essential for autophagosome formation and important for regulation of size
1398 and distribution of lipid droplets. *MBoC*. 23:896–909. doi:10.1091/mbc.e11-09-0785.

1399 Voeltz, G.K., E.M. Sawyer, G. Hajnóczky, and W.A. Prinz. 2024. Making the connection: How
1400 membrane contact sites have changed our view of organelle biology. *Cell*. 187:257–270.
1401 doi:10.1016/j.cell.2023.11.040.

1402 Wang, C., B. Wang, T. Pandey, Y. Long, J. Zhang, F. Oh, J. Sima, R. Guo, Y. Liu, C. Zhang, S.
1403 Mukherjee, M. Bassik, W. Lin, H. Deng, G. Vale, J.G. McDonald, K. Shen, and D.K. Ma.
1404 2022. A conserved megaprotein-based molecular bridge critical for lipid trafficking and
1405 cold resilience. *Nat Commun*. 13:6805. doi:10.1038/s41467-022-34450-y.

1406 Wang, C.-W., J. Kim, W.-P. Huang, H. Abeliovich, P.E. Stromhaug, W.A. Dunn, and D.J. Klionsky.
1407 2001. Apg2 Is a Novel Protein Required for the Cytoplasm to Vacuole Targeting,

Autophagy, and Pexophagy Pathways *. *Journal of Biological Chemistry*. 276:30442–30451. doi:10.1074/jbc.M102342200.

Wang, G., S. Nola, S. Bovio, P. Bun, M. Coppey-Moisan, F. Lafont, and T. Galli. 2018. Biomechanical Control of Lysosomal Secretion Via the VAMP7 Hub: A Tug-of-War between VARP and LRRK1. *iScience*. 4:127–143. doi:10.1016/j.isci.2018.05.016.

Wang, X., P. Xu, A. Bentley-DeSousa, W. Hancock-Cerutti, S. Cai, B.T. Johnson, F. Tonelli, G. Talaia, D.R. Alessi, S.M. Ferguson, and P.D. Camilli. 2024a. Lysosome damage triggers acute formation of ER to lysosomes membrane tethers mediated by the bridge-like lipid transport protein VPS13C. 2024.06.08.598070. doi:10.1101/2024.06.08.598070.

Wang, Y., S. Dahmane, R. Ti, X. Mai, L. Zhu, L.-A. Carlson, and G. Stjepanovic. 2024b. Structural basis for lipid transfer by the ATG2A–ATG9A complex. *Nat Struct Mol Biol*. 1–13. doi:10.1038/s41594-024-01376-6.

Wang, Y., W. Huynh, T.D. Skokan, W. Lu, A. Weiss, and R.D. Vale. 2019. CRACR2a is a calcium-activated dynein adaptor protein that regulates endocytic traffic. *Journal of Cell Biology*. 218:1619–1633. doi:10.1083/jcb.201806097.

Wen, L., L. Liu, X. Shen, H. Li, Z. Zhu, H. Huang, M. Cai, D. Qian, S. Shen, Y. Qiu, Y. Cui, and Y. Sheng. 2020. The association of the UHRF1BP1 gene with systemic lupus erythematosus was replicated in a Han Chinese population from mainland China. *Annals of Human Genetics*. 84:221–228. doi:10.1111/ahg.12362.

Wirtz, K.W.A. 1991. Phospholipid transfer proteins: From lipid monolayers to cells. *Klin Wochenschr*. 69:105–111. doi:10.1007/BF01795953.

Wong, L.H., A.T. Gatta, and T.P. Levine. 2019. Lipid transfer proteins: the lipid commute via shuttles, bridges and tubes. *Nat Rev Mol Cell Biol*. 20:85–101. doi:10.1038/s41580-018-0071-5.

Xu, C.S., K.J. Hayworth, Z. Lu, P. Grob, A.M. Hassan, J.G. García-Cerdán, K.K. Niyogi, E. Nogales, R.J. Weinberg, and H.F. Hess. 2017. Enhanced FIB-SEM systems for large-volume 3D imaging. *eLife*. 6:e25916. doi:10.7554/eLife.25916.

Xu, C.S., S. Pang, G. Shtengel, A. Müller, A.T. Ritter, H.K. Hoffman, S. Takemura, Z. Lu, H.A. Pasolli, N. Iyer, J. Chung, D. Bennett, A.V. Weigel, M. Freeman, S.B. van Engelenburg, T.C. Walther, R.V. Farese, J. Lippincott-Schwartz, I. Mellman, M. Solimena, and H.F. Hess. 2021. An open-access volume electron microscopy atlas of whole cells and tissues. *Nature*. 599:147–151. doi:10.1038/s41586-021-03992-4.

Yang, J., I. Anishchenko, H. Park, Z. Peng, S. Ovchinnikov, and D. Baker. 2020. Improved protein structure prediction using predicted interresidue orientations. *PNAS*. 117:1496–1503. doi:10.1073/pnas.1914677117.

Yariv, B., E. Yariv, A. Kessel, G. Masrati, A.B. Chorin, E. Martz, I. Mayrose, T. Pupko, and N. Ben-Tal. 2023. Using evolutionary data to make sense of macromolecules with a “face-lifted” ConSurf. *Protein Science*. 32:e4582. doi:10.1002/pro.4582.

1446 Zhang, Y., W. Yang, C.C. Mok, T.M. Chan, R.W.S. Wong, M.Y. Mok, K.W. Lee, S.N. Wong,
1447 A.M.H. Leung, T.L. Lee, M.H.K. Ho, P.P.W. Lee, W.H.S. Wong, J. Yang, J. Zhang, C.-M.
1448 Wong, I.O.L. Ng, M.-M. Garcia-Barceló, S.S. Cherny, P.K.-H. Tam, P.C. Sham, C.S. Lau,
1449 and Y.L. Lau. 2011. Two missense variants in UHRF1BP1 are independently associated
1450 with systemic lupus erythematosus in Hong Kong Chinese. *Genes Immun*. 12:231–234.
1451 doi:10.1038/gene.2010.66.

1452

Figure 1

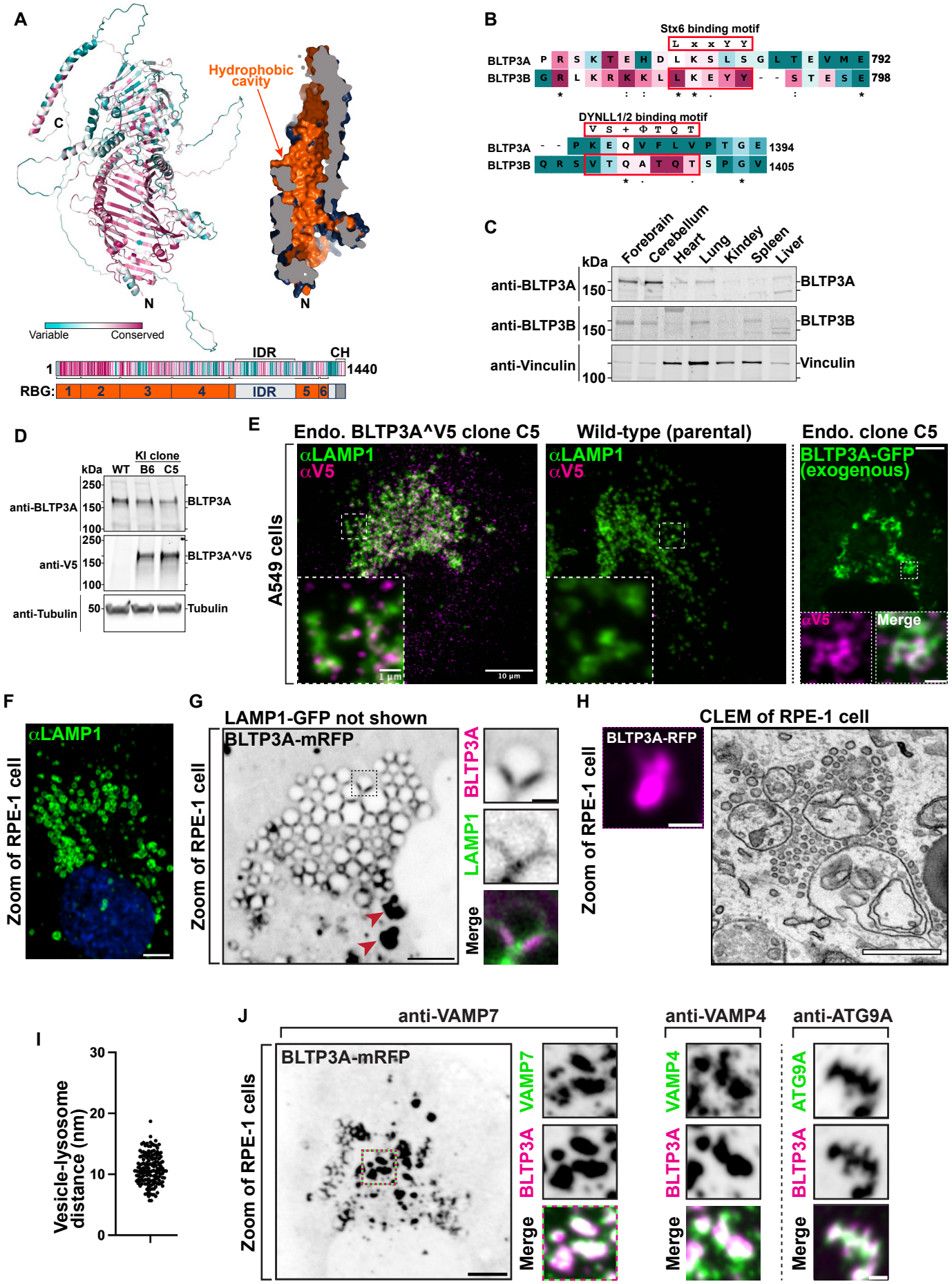
A
Hydrophobic cavity
C
N
N
Variable
Conserved
IDR
CH
1
1440
RBG:
1
2
3
4
IDR
5
6
B
Stx6 binding motif
L x x Y Y
BLTP3A P R S K T E H D L K S L S G L T E V M E 792
BLTP3B G R L K R K K L L K E Y Y - - S T E S E 798
DYNLL1/2 binding motif
V S + Φ T Q T
BLTP3A - - P K E Q V F L V P T G E 1394
BLTP3B Q R S V T Q A T Q T S P G V 1405
C
Forebrain
Cerebellum
Heart
Lung
Kindey
Spleen
Liver
kDa
anti-BLTP3A
150
BLTP3A
anti-BLTP3B
150
BLTP3B
anti-Vinculin
100
Vinculin
D
KI clone
kDa
WT
B6
C5
anti-BLTP3A
250
150
100
BLTP3A
anti-V5
250
150
100
BLTP3A^V5
anti-Tubulin
50
Tubulin
E
Endo. BLTP3A^V5 clone C5
Wild-type (parental)
Endo. clone C5
A549 cells
αLAMP1
αV5
αLAMP1
αV5
BLTP3A-GFP
(exogenous)
αV5
Merge
1 µm
10 µm
F
Zoom of RPE-1 cell
αLAMP1
G
LAMP1-GFP not shown
Zoom of RPE-1 cell
BLTP3A-mRFP
BLTP3A
LAMP1
Merge
H
CLEM of RPE-1 cell
Zoom of RPE-1 cell
BLTP3A-RFP
I
Vesicle-lysosome distance (nm)
30
20
10
0
J
anti-VAMP7
anti-VAMP4
anti-ATG9A
Zoom of RPE-1 cells
BLTP3A-mRFP
VAMP7
BLTP3A
Merge
VAMP4
BLTP3A
Merge
ATG9A
BLTP3A
Merge

Figure 2

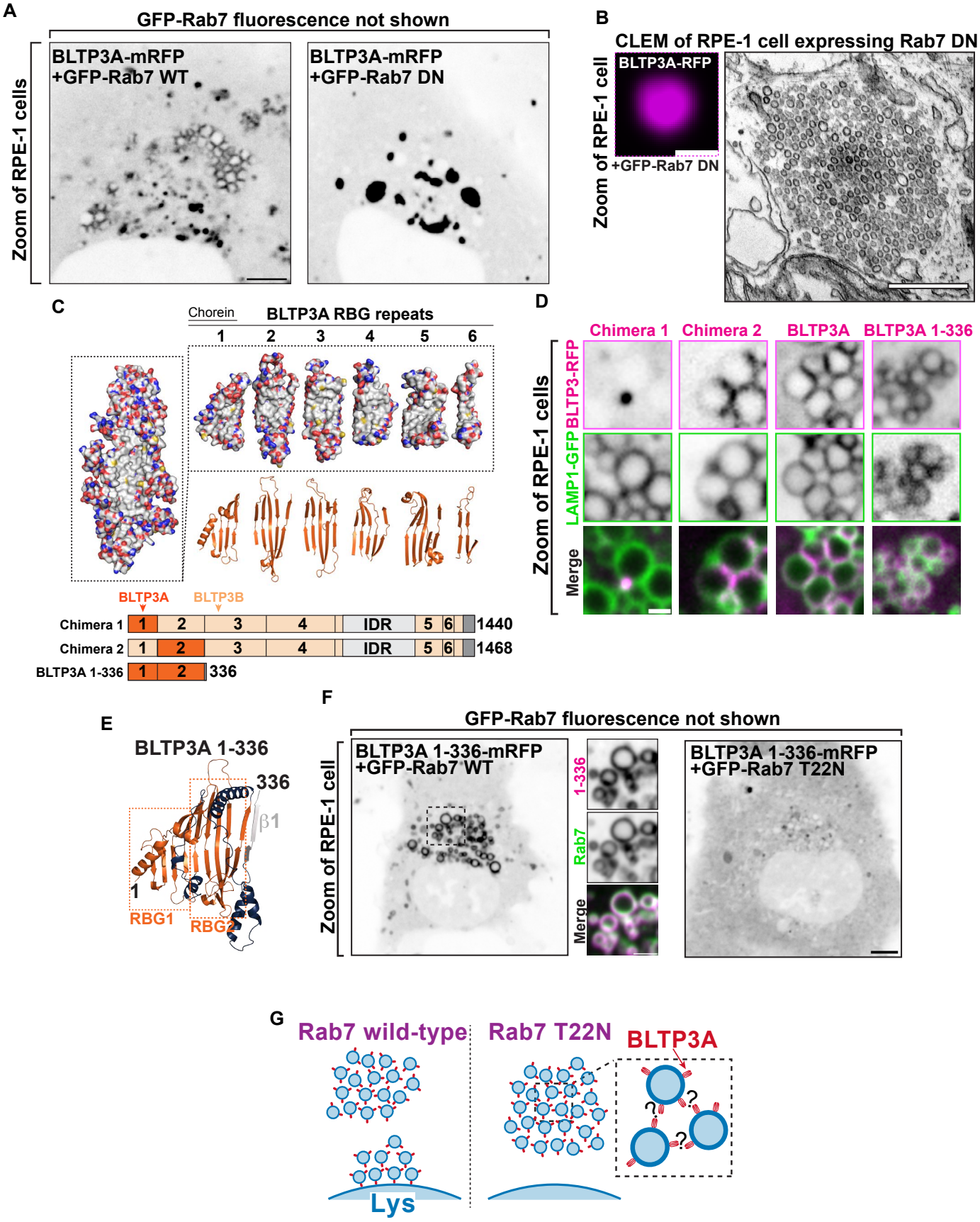
A
GFP-Rab7 fluorescence not shown
Zoom of RPE-1 cells
BLTP3A-mRFP
+GFP-Rab7 WT
BLTP3A-mRFP
+GFP-Rab7 DN
B
CLEM of RPE-1 cell expressing Rab7 DN
Zoom of RPE-1 cell
BLTP3A-RFP
+GFP-Rab7 DN
C
Chorein
BLTP3A RBG repeats
1 2 3 4 5 6
BLTP3A
BLTP3B
Chimera 1 1 2 3 4 IDR 5 6 1440
Chimera 2 1 2 3 4 IDR 5 6 1468
BLTP3A 1-336 1 2 336
D
Chimera 1
Chimera 2
BLTP3A
BLTP3A 1-336
Zoom of RPE-1 cells
BLTP3-RFP
LAMP1-GFP
Merge
E
BLTP3A 1-336
336
β1
1
RBG1
RBG2
F
GFP-Rab7 fluorescence not shown
Zoom of RPE-1 cell
BLTP3A 1-336-mRFP
+GFP-Rab7 WT
1-336
Rab7
Merge
BLTP3A 1-336-mRFP
+GFP-Rab7 T22N
G
Rab7 wild-type
Rab7 T22N
BLTP3A
Lys

Figure 3

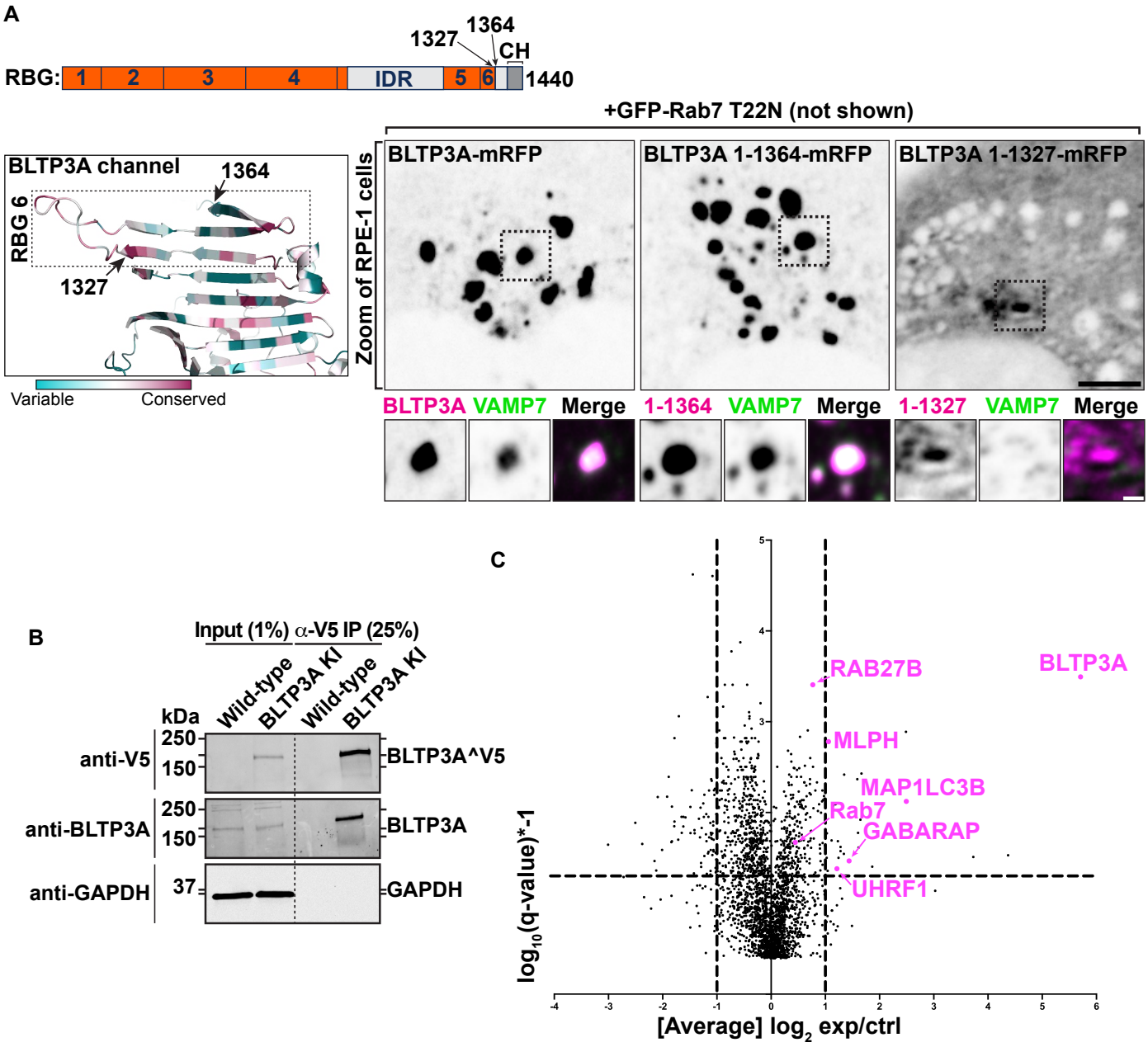
A
1327
1364
CH
RBG:
1
2
3
4
IDR
5
6
1440
+GFP-Rab7 T22N (not shown)
BLTP3A channel
1364
RBG 6
1327
Variable
Conserved
Zoom of RPE-1 cells
BLTP3A-mRFP
BLTP3A 1-1364-mRFP
BLTP3A 1-1327-mRFP
BLTP3A VAMP7 Merge
1-1364 VAMP7 Merge
1-1327 VAMP7 Merge
B
Input (1%) α-V5 IP (25%)
Wild-type
BLTP3A KI
Wild-type
BLTP3A KI
kDa
anti-V5
250
150
BLTP3A^V5
anti-BLTP3A
250
150
BLTP3A
anti-GAPDH
37
GAPDH
C
RAB27B
BLTP3A
MLPH
MAP1LC3B
Rab7
GABARAP
UHRF1
log10(q-value)*-1
[Average] log2 exp/ctrl

Figure 4

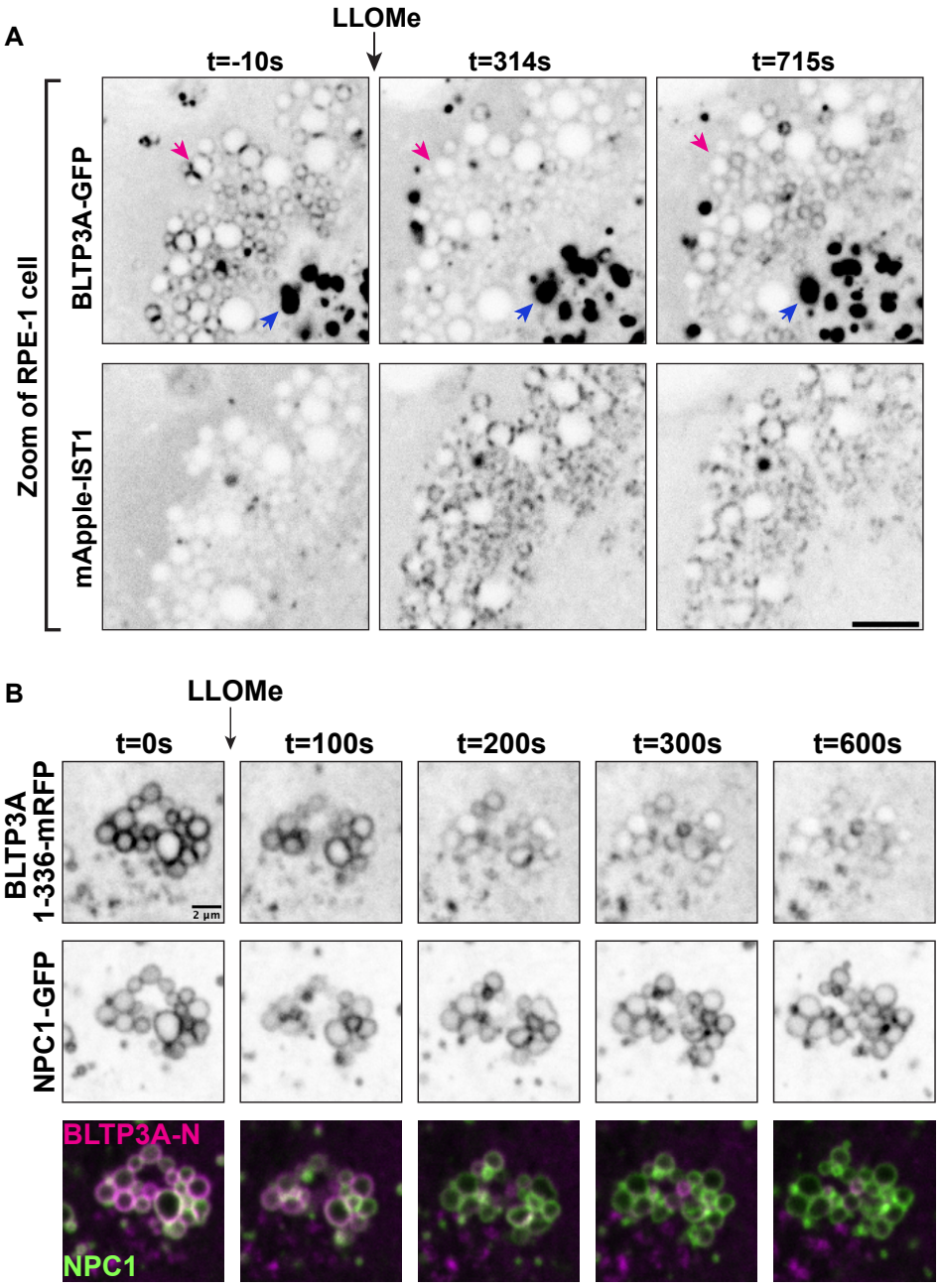
A
LLOMe
t=-10s
t=314s
t=715s
Zoom of RPE-1 cell
BLTP3A-GFP
mApple-IST1
B
LLOMe
t=0s
t=100s
t=200s
t=300s
t=600s
BLTP3A 1-336-mRFP
2 µm
NPC1-GFP
BLTP3A-N
NPC1

Figure 5

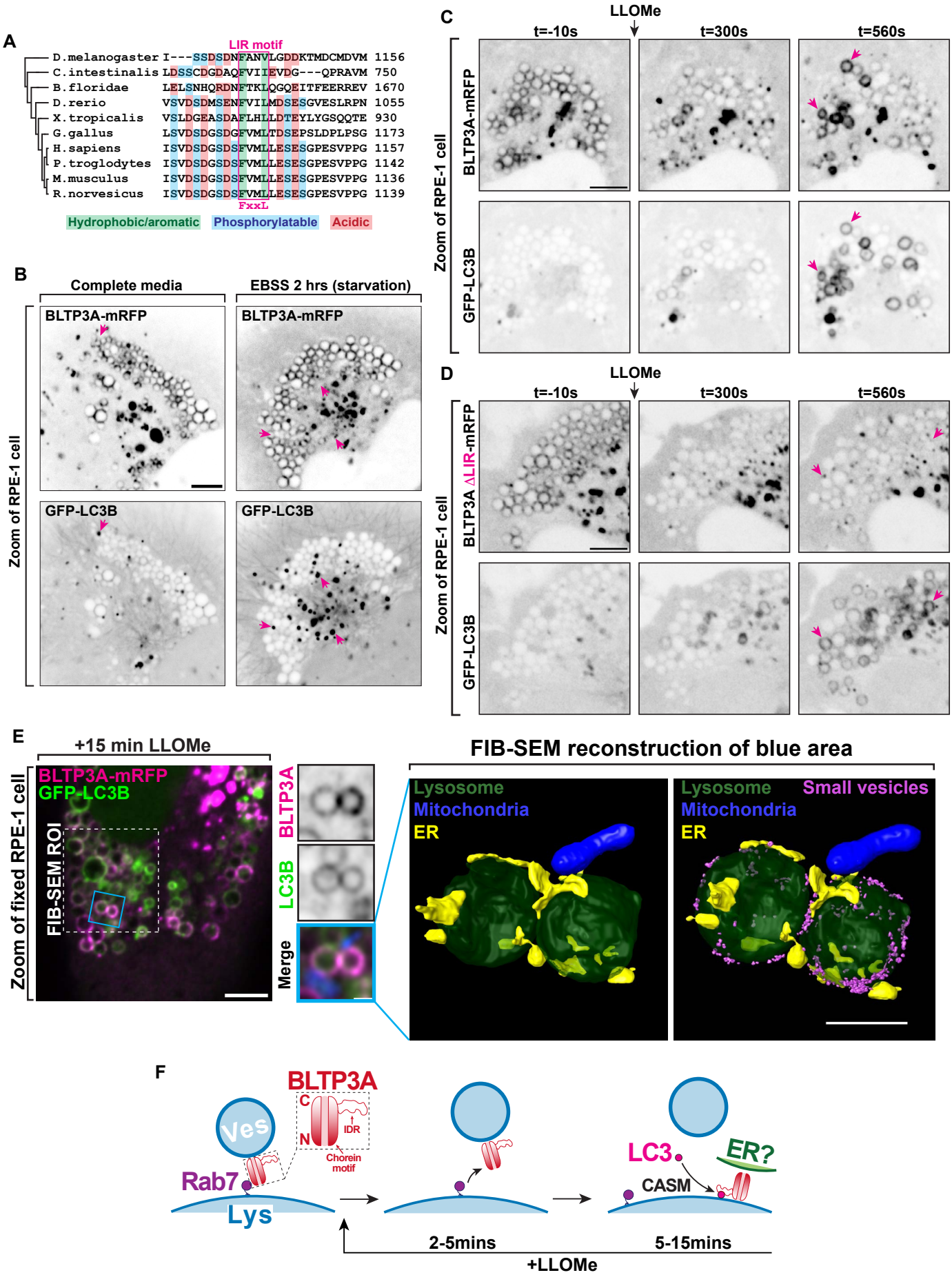
A
LIR motif
D.melanogaster I---SSDSDNFANVLGDDKTMDCMDVM 1156
C.intestinalis LDSSCDGDAQFVIIEVDG---QPRAVM 750
B.floridae LELSNHQRDNFTKLQGQEITFEERREV 1670
D.rerio VSVDSDMSENFVILMDSESGVESLRPN 1055
X.tropicalis VSLDGEASDAFLHLLDTEYLYGSQQTE 930
G.gallus LSVDSDGSDGFVMLTDSEPSLDPLPSG 1173
H.sapiens ISVDSDGSDSFVMLLESESGPESVPPG 1157
P.troglodytes ISVDSDGSDSFVMLLESESGPESVPPG 1142
M.musculus ISVDSDGSDSFVMLLESESGPESVPPG 1136
R.norvesicus ISVDSDGSDSFVMLLESESGPESVPPG 1139
FxxL
Hydrophobic/aromatic
Phosphorylatable
Acidic
B
Complete media
EBSS 2 hrs (starvation)
Zoom of RPE-1 cell
BLTP3A-mRFP
GFP-LC3B
C
LLOMe
t=-10s
t=300s
t=560s
Zoom of RPE-1 cell
BLTP3A-mRFP
GFP-LC3B
D
LLOMe
t=-10s
t=300s
t=560s
Zoom of RPE-1 cell
BLTP3A ΔLIR-mRFP
GFP-LC3B
E
+15 min LLOMe
Zoom of fixed RPE-1 cell
BLTP3A-mRFP
GFP-LC3B
FIB-SEM ROI
BLTP3A
LC3B
Merge
FIB-SEM reconstruction of blue area
Lysosome
Mitochondria
ER
Lysosome
Small vesicles
Mitochondria
ER
F
BLTP3A
C
N
IDR
Chorein motif
Ves
Rab7
Lys
LC3
ER?
CASM
2-5mins
5-15mins
+LLOMe

Figure 6

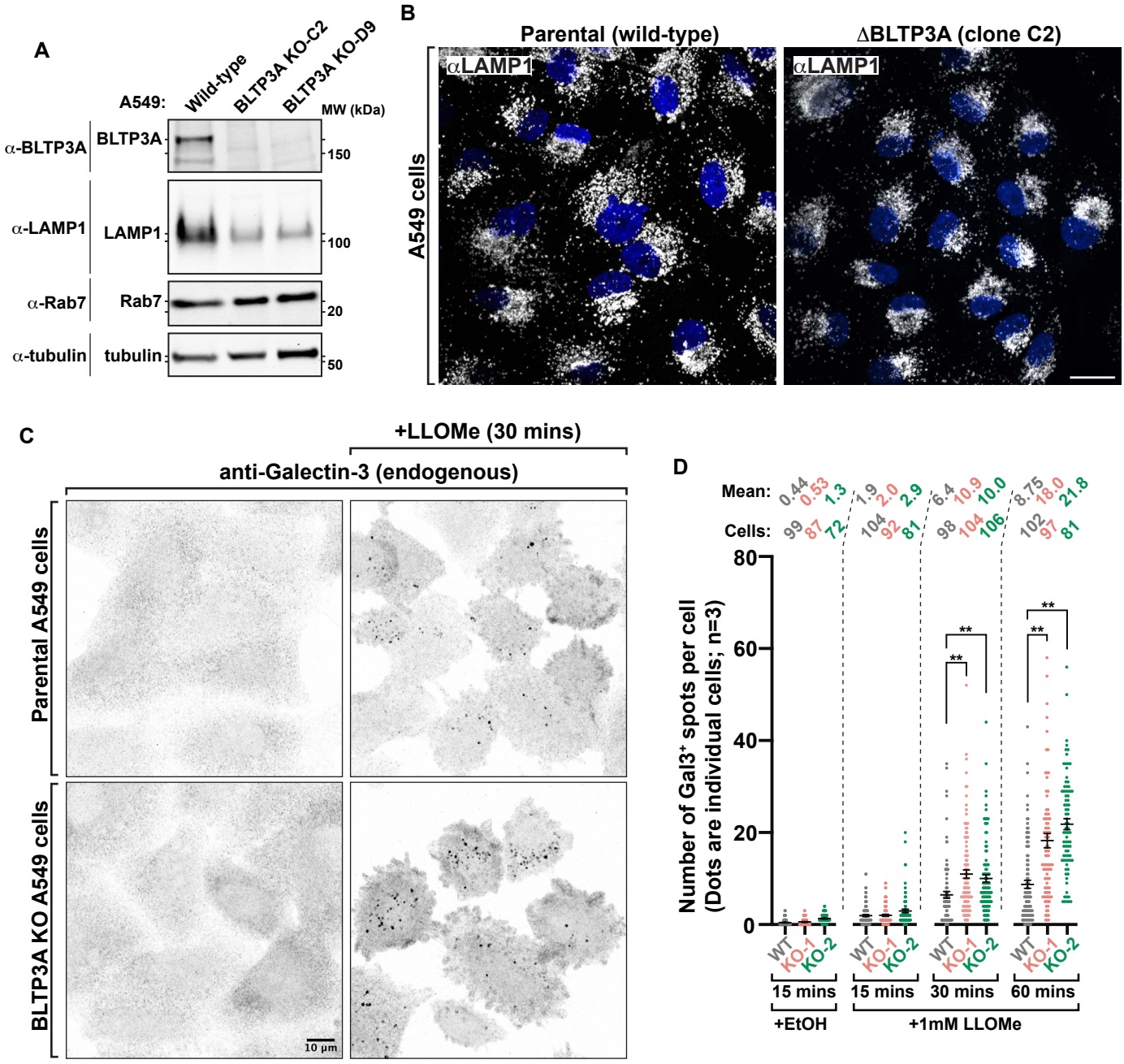
A
A549:
Wild-type
BLTP3A KO-C2
BLTP3A KO-D9
MW (kDa)
α-BLTP3A
BLTP3A
150
α-LAMP1
LAMP1
100
α-Rab7
Rab7
20
α-tubulin
tubulin
50
B
Parental (wild-type)
ΔBLTP3A (clone C2)
αLAMP1
αLAMP1
A549 cells
C
+LLOMe (30 mins)
anti-Galectin-3 (endogenous)
Parental A549 cells
BLTP3A KO A549 cells
10 µm
D
Mean: 0.44 0.53 1.3 1.9 2.0 2.9 6.4 10.9 10.0 8.75 18.0 21.8
Cells: 99 87 72 104 92 81 98 104 106 102 97 81
Number of Gal3⁺ spots per cell
(Dots are individual cells; n=3)
80
60
40
20
0
**
WT
KO-1
KO-2
15 mins
15 mins
30 mins
60 mins
+EtOH
+1mM LLOMe

Supplemental Figure 1

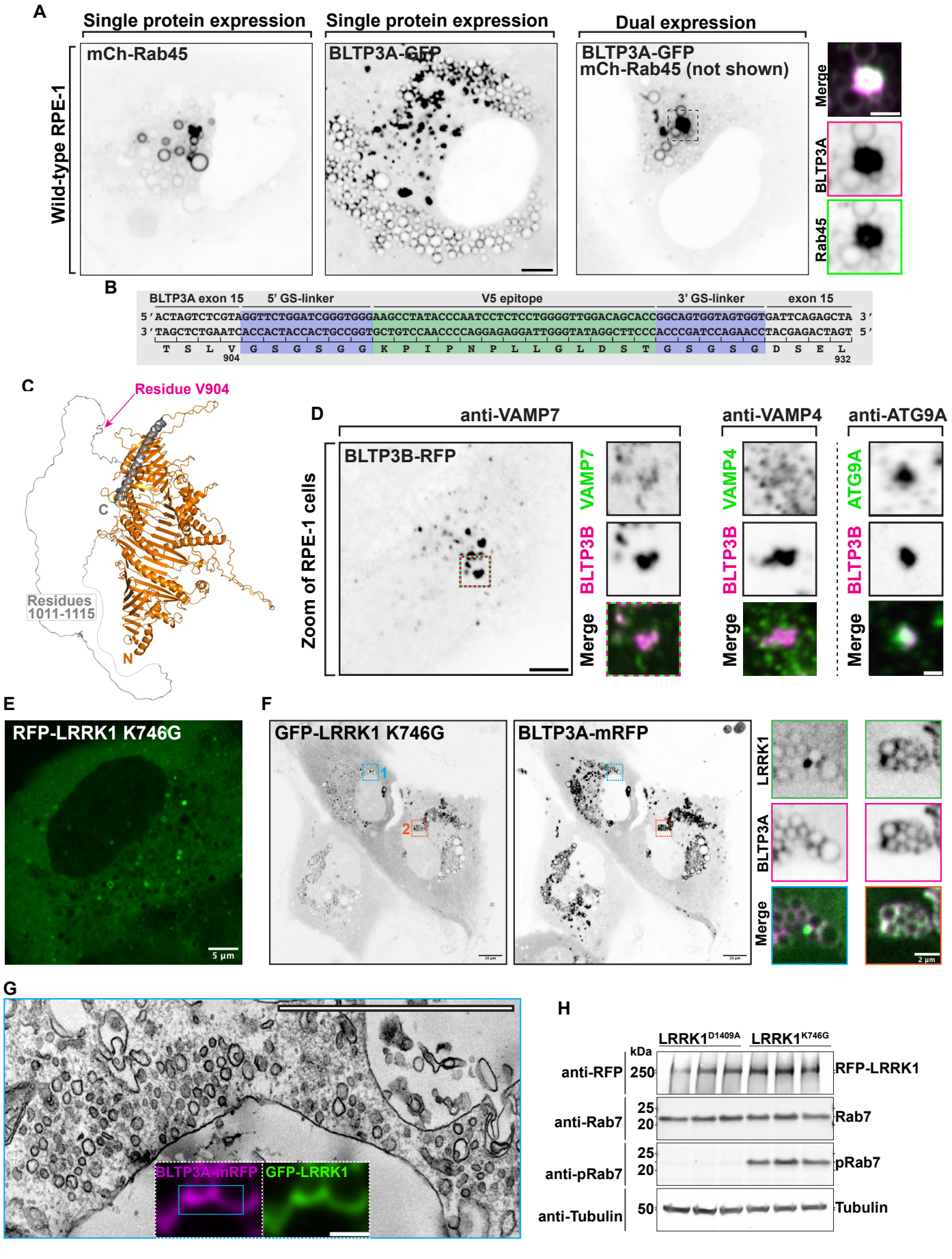

Supplemental Figure 2

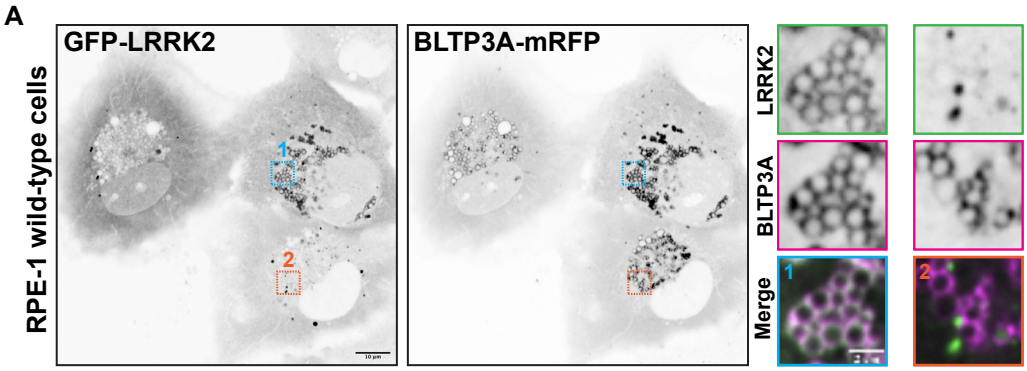

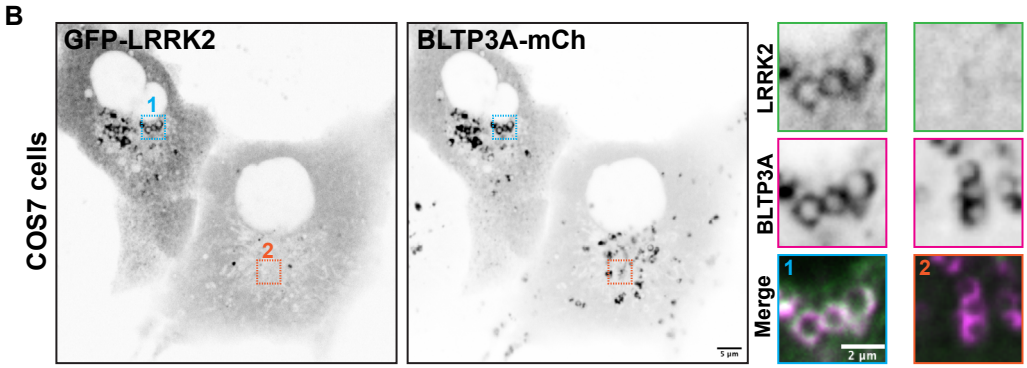

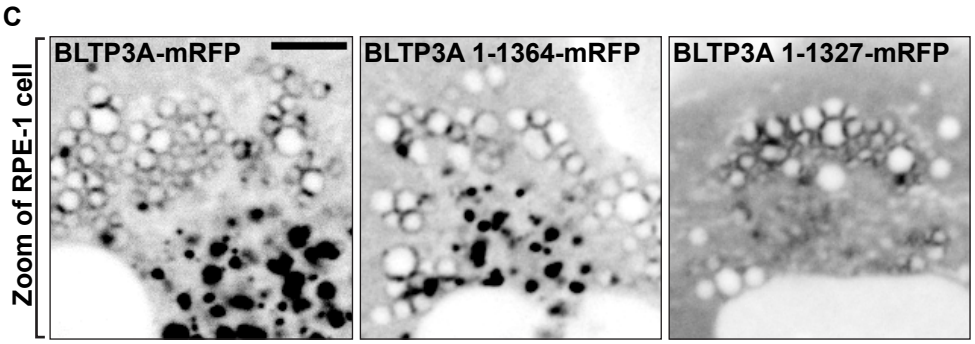

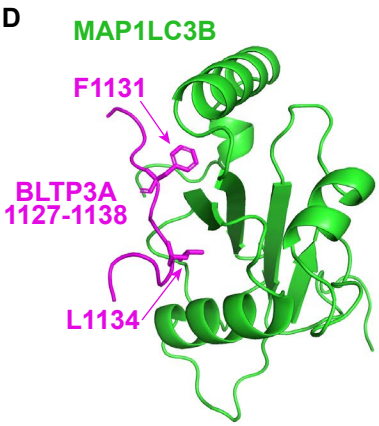

E

AF3 predictions of BLTP3A with mAtg8 proteins

BLTP3A:	1110-1150		1110-1150 ΔLIR	
	ipTM	pTM	ipTM	pTM
MAP1LC3A	0.66	0.7	0.31	0.69
MAP1LC3B	0.56	0.68	0.32	0.7
MAP1LC3C	0.57	0.62	0.32	0.62
GABARAP	0.74	0.76	0.55	0.74
GABARAPL1	0.73	0.75	0.52	0.72
GABARAPL2	0.72	0.74	0.53	0.73
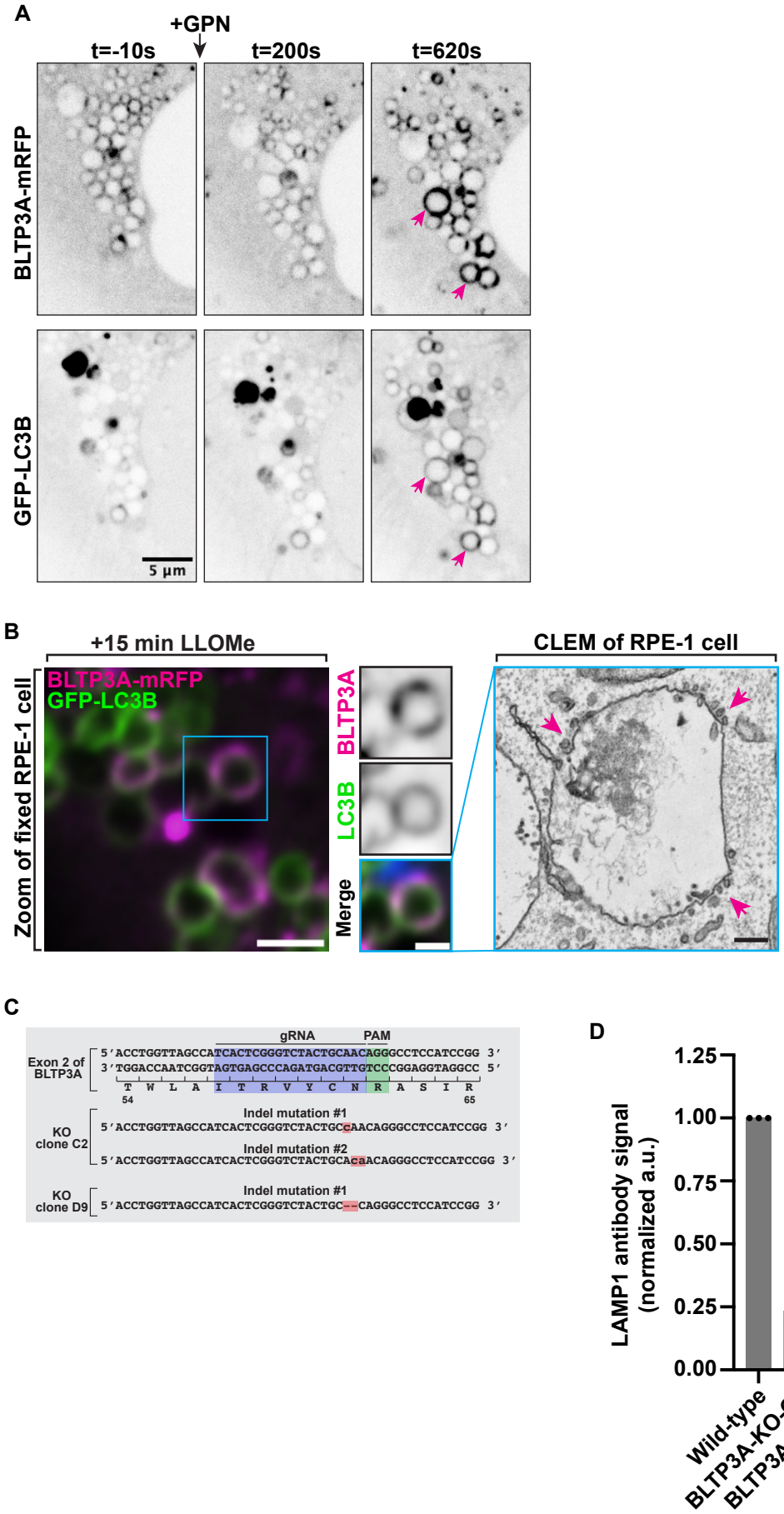
Supplemental Figure 3